

MAPPING EXTREMELY LOW METALLICITY GALAXIES TO REDSHIFT ONE¹

YUKO KAKAZU,² LENNOX L. COWIE,² AND ESTHER M. HU²

Received 2007 April 3; accepted 2007 June 15

ABSTRACT

We describe the results of a narrowband search for ultrastrong emission line galaxies (USELs) with $\text{EW}(\text{H}\beta) \geq 30 \text{ \AA}$. A total of 542 candidate galaxies are found in a one-half square degree survey using two $\sim 120 \text{ \AA}$ filters centered at 8150 and 9140 \AA with Subaru SuprimeCam. Follow-up spectroscopy for randomly selected objects in the candidate sample with Keck II DEIMOS shows that they consist of $[\text{O III}] \lambda 5007$ –, $[\text{O II}] \lambda 3727$ –, and $\text{H}\alpha$ –selected strong emission line galaxies at intermediate redshift ($z < 1$) and $\text{Ly}\alpha$ –emitting galaxies at high redshift ($z \gg 5$). We determine the $\text{H}\beta$ luminosity functions and the star formation density of the USELs, which is 5%–10% of the value found from ultraviolet continuum objects at $z = 0$ –1, suggesting that they correspond to a major epoch in the galaxy formation process at these redshifts. Many of the USELs show the temperature-sensitive $[\text{O III}] \lambda 4363$ auroral lines, and about a dozen have oxygen abundances satisfying the criteria of extremely metal-poor galaxies (XMPGs). These XMPGs are the most distant known today. Our high yield rate of XMPGs suggests that the narrowband method is a powerful way to find such populations. Moreover, the lowest metallicity measured in our sample is close to the minimum metallicity found in local galaxies [$12 + \log (\text{O}/\text{H}) \sim 7.1$], although we need deeper spectra to minimize the errors. *HST* ACS images of several USELs exhibit widespread morphologies from relatively compact high surface brightness objects to very diffuse low surface brightness ones. The luminosities, metallicities, and star formation rates of USELs are consistent with the strong emitters being start-up intermediate-mass galaxies that will evolve into more normal galaxies and suggest that galaxies are still forming in relatively chemically pristine sites at $z < 1$.

Subject headings: cosmology: observations — galaxies: abundances — galaxies: distances and redshifts — galaxies: evolution — galaxies: starburst

Online material: color figures

1. INTRODUCTION

The study of low-metallicity galaxies is of considerable interest for the clues that it can provide about the first stages of galaxy formation and chemical enrichment. We would also like to know if there are any genuinely young galaxies undergoing their first episodes of star formation at low redshifts. To date, the most metal-poor systems studied have been the blue compact emission-line galaxies found in the local universe, with systems such as I Zw 18 and SBS 0335–052W defining the low-metallicity boundary with measured $12 + \log (\text{O}/\text{H})$ of ~ 7.1 – 7.2 (Sargent & Searle 1970; Thuan & Izotov 2005; Izotov et al. 2005). More recently, the Sloan Digital Sky Survey (SDSS) has yielded additional extremely metal-poor galaxies [XMPGs; $12 + \log (\text{O}/\text{H}) < 7.65$ or $Z < Z_{\odot}/12$; Kniazev et al. 2003; Izotov et al. 2006a]. Despite enormous efforts, only a few dozen such XMPGs are known, all at redshift $z < 0.05$ (e.g., Oey 2006; Izotov 2006).

Historically, objective prism surveys have been used to select emission-line galaxies for low-metallicity studies (e.g., the Hamburg QSO Survey [Popescu et al. 1996] and its HSS sequel [Ugryumov et al. 1999] that discovered HS 2134+0400 [Pustilnik et al. 2006] and the Kitt Peak International Spectroscopy Survey [KISS; Salzer et al. 2000; Melbourne & Salzer 2002]). The advantage of using the objective prism technique rather than the

continuum selection, employed with the SDSS (Kniazev et al. 2003) or DEEP2 surveys (Hoyos et al. 2005), is that they have a higher efficiency and provide a more uniform selection. By comparison, continuum/broadband surveys have a very low yield rate (eight new XMPGs and four recovered XMPGs from an analysis of 250,000 spectra over $\sim 3000 \text{ deg}^2$ for the SDSS; Kniazev et al. 2003), since low-metallicity populations in their first outburst have weak continua and strong emission lines.

An alternative method of discovering strong emission line, low-metallicity galaxies is to use narrowband surveys. Strong emission line galaxies have historically been picked up in high- z $\text{Ly}\alpha$ searches (e.g., Stockton & Ridgway 1998; Hu et al. 1998, 2004; Stern et al. 2000; Tran et al. 2004; Ajiki et al. 2006) where they have been considered contaminants. However, the low-redshift emission-line galaxies seen in these surveys are of great interest in their own right, as we show in the present paper. While some spectroscopic studies have been carried out for low-redshift galaxies selected from narrowband surveys (e.g., Maier et al. 2006; Ly et al. 2007), the small sample sizes have precluded any detailed investigation of metallicity and identification of a low-metallicity population.

The narrowband method probes to much deeper limits than the objective prism surveys. This enables probing star-forming populations out to near redshift $z \sim 1$ where the cosmic star formation rates (SFRs) are considerably higher. Furthermore, the narrowband emission line selection allows us to assemble very large samples of strong emission line objects, with a clean selection of different line types for the construction of luminosity functions.

Such a sample allows us to address such questions as whether there are substantial populations of strong star-forming galaxies with low metallicities among more massive galaxies. There

¹ Based in part on data obtained at the Subaru Telescope, which is operated by the National Astronomical Observatory of Japan. Based in part on data obtained at the W. M. Keck Observatory, which is operated as a scientific partnership among the California Institute of Technology, the University of California, and NASA and was made possible by the generous financial support of the W. M. Keck Foundation.

² Institute for Astronomy, University of Hawaii, Honolulu, HI 96822; kakazu@ifa.hawaii.edu, cowie@ifa.hawaii.edu, hu@ifa.hawaii.edu.

TABLE 1
NARROWBAND SURVEY AREA COVERAGE

Field	R.A. (J2000.0)	Decl. (J2000.0)	(l^{II} , b^{II})	E_{B-V}^a	NB816 (arcmin ²)	NB912 (arcmin ²)
SSA22	22 17 57.00	+00 14 54.5	(63.1, -44.1)	0.07	674	591
SSA22_new	22 18 24.67	+00 36 53.4	(63.6, -43.9)	0.06	278	278
A370_new	02 41 16.27	-01 34 25.1	(173.4, -53.3)	0.03	278	278
HDF-N	12 36 49.57	+62 12 54.0	(125.9, +54.8)	0.01	710	528
Total	1940	1675

NOTES.— Units of right ascension are hours, minutes, and seconds, and units of declination are degrees, arcminutes, and arcseconds. An adjacent field to A370_new is a site of a gravitational lensing cluster at $z \sim 0.375$ and was omitted from the survey.

^a Estimated using <http://irsa.ipac.caltech.edu/applications/DUST/> based on Schlegel et al. (1998).

has been considerable controversy about the interpretation of the low-metallicity measurements in the blue compact galaxy samples, where the ease with which gas may be ejected in these dwarf galaxies has complicated the picture (e.g., Corbin et al. 2006) or, at least, resulted in identifying low-metallicity systems that are not forming their first generation of stars. The identification of low-metallicity galaxies, at the level of the XMPGs, among massive galaxies may provide less ambiguous examples of galaxies that are genuinely “young” and caught in the initial stages of star formation. Current efforts to identify low-metallicity galaxies from continuum-selected surveys (e.g., Kobulnicky et al. 2003; Lilly et al. 2003; Kobulnicky & Kewley 2004; Hoyos et al. 2005) have low-metallicity thresholds that are higher than this, about one-third solar (in O/H). With a narrowband selection criterion much larger emission-line samples including very low metallicity galaxies can be identified. With these large samples it is also possible to determine whether there is an observed lower metallicity threshold for such galaxies and to estimate what the contribution of such strong star formers might be at these epochs.

In the present work we use a number of deep, narrowband images obtained with the SuprimeCam mosaic CCD camera (Miyazaki et al. 2002) on the Subaru 8.2 m telescope to find a large sample of extreme emission line galaxies. We first (§ 2) outline the selection criteria (magnitude and flux thresholds) for the target fields resulting in a sample of 542 galaxies, which we call USELs (ultrastrong emission line galaxies). We then describe (§ 3) the spectroscopic follow-ups for 161 of these galaxies using multiobject masks with DEIMOS (Faber et al. 2003) on the 10 m Keck II telescope. Sample spectra for each class of object are shown. Flux calibration and equivalent width distributions are presented in § 4, and the resulting measured line ratios are discussed. In § 5 luminosity functions are constructed and SFRs are estimated for the sample. These galaxies are estimated to contribute roughly 10% to the measured SFR (without extinction corrections) at this epoch. Analysis of the metallicities is given in § 6. Their morphologies are discussed in § 7, and a final summary discussion is given in § 8. We use a standard $H_0 = 70 \text{ km s}^{-1} \text{ Mpc}^{-1}$, $\Omega_m = 0.3$, $\Omega_\Lambda = 0.7$ cosmology throughout.

2. THE NARROWBAND SELECTION

The emission-line sample was chosen from a set of narrowband images obtained with the SuprimeCam camera on the Subaru 8.2 m telescope. The data were obtained in a number of runs between 2001 and 2005 under photometric or near-photometric conditions. We used two $\sim 120 \text{ \AA}$ (FWHM) filters centered at nominal wavelengths of 8150 and 9140 \AA in regions of low sky background between the OH bands. The nominal spec-

ifications for the Subaru filters may be found online³ and are also described in Ajiki et al. (2003). We refer to these filters as NB816 and NB912.

Roughly 5 hr exposures were obtained with NB816 and ~ 10 hr exposures with NB912, yielding 5σ limits fainter than 26 mag in both bands. Deep exposures in B , V , R , I , and z' were also taken for the fields. The data were taken as a sequence of dithered background-limited exposures, and successive mosaic sequences were rotated by 90° . Only the central uniformly covered areas of the images were used. Corresponding continuum exposures were always obtained in the same observing run as the narrowband exposures to avoid false identifications of transients such as high- z supernovae, or Kuiper Belt objects, as emission-line candidates. A detailed description of the full reduction procedure for images is given in Capak et al. (2004). All magnitudes are given in the AB system (Oke 1990). These were measured in $3''$ diameter apertures and had average aperture corrections applied to give total magnitudes.

The primary purpose of the program was to study Ly α emitters at redshifts of $z \sim 5.7$ and $z \sim 6.5$ (Hu et al. 2004; E. M. Hu et al. 2007, in preparation), but the narrowband imaging is also ideal for selecting lower redshift emission-line galaxies, and it is for this purpose that we use these data in the present paper. The fields that we use and the area covered (approximately one-half square degree in each bandpass) are summarized in Table 1. These are distributed over the sky to deal with cosmic variance. We selected galaxies in the narrowband NB816 filter using the Cousins I -band filter as a reference continuum bandpass and including all galaxies with $\text{NB816} < 25$ and $I - \text{NB816}$ greater than 0.8. We selected galaxies in the NB912 filter with the z filter as the reference continuum bandpass and including all galaxies with $\text{NB912} < 25$ and $z - \text{NB912}$ greater than 1. The selection process is illustrated for a galaxy found in the NB912 filter in Figure 1. Both selections correspond roughly to choosing objects with emission lines with rest-frame equivalent widths greater than 100 \AA . The exact equivalent width limit depends on the precise position of the emission line in the filter and the redshift of the galaxy, which in turn depends on which emission line is producing the excess light in the narrow band.

The final USEL sample consists of 542 galaxies (267 in the NB816 filter and 275 in the NB912 filter). Tabulated coordinates, multicolor magnitudes, and redshifts (where measured) for these objects are summarized in Tables 2 and 3. Very few of these objects would be included in continuum-selected spectroscopic samples. Figure 2 shows the narrowband excess as a function of narrowband (N_{AB}) magnitude for objects with narrowband magnitudes

³ See <http://www.naoj.org/Observing/Instruments/SCam/sensitivity.html>.

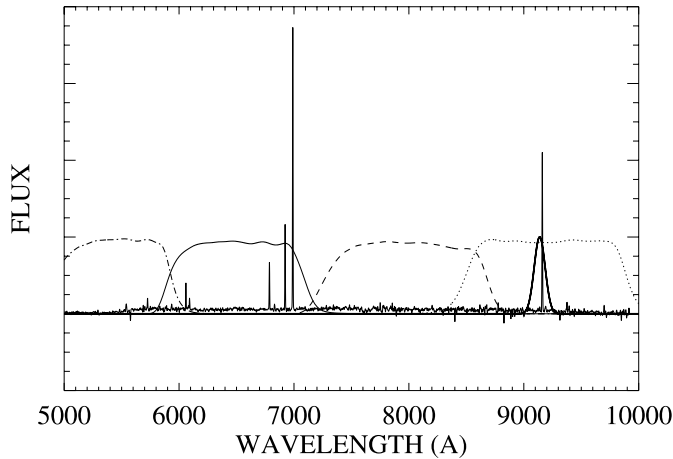


FIG. 1.— Schematic illustration of the selection process and a typical spectrum of the galaxies we find. The objects are chosen based on their excess light in one of two narrowband filters at 8150 and 9140 Å. The present case corresponds to an $H\alpha$ emission line object found in the 9140 Å filter (shown with the narrow solid line). Also illustrated are the broadband V (dot-dashed line), R (solid line), I (dashed line), and z' (dotted line) filters used to measure the continuum. The spectrum shown corresponds to object 205 in Table 3 and is an $H\alpha$ emitter at $z = 0.3981$. The easily visible lines are the Balmer series and the $[O III]$ lines at 5007, 4959, and 4363 Å.

brighter than 24. The open symbols show the present sample, while the filled symbols show objects that would be included in an $R < 24$ continuum-selected sample.

3. SPECTRA

Spectroscopic observations were obtained for 161 USELs from the sample using the Deep Extragalactic Imaging Multi-Object Spectrograph (DEIMOS; Faber et al. 2003) on Keck II in a series of runs between 2003 and 2006. The emission-line objects were included in masks designed to observe high- z $Ly\alpha$ candidates and, as can be seen in the bottom panel of Figure 2, constitute an essentially random sample of the emission-line galaxies.

The observations were primarily made with the G830 line mm^{-1} grating blazed at 8640 Å and used 1" wide slitlets. In this configuration, the resolution is 3.3 Å, which is sufficient to distinguish the $[O II] \lambda 3727$ doublet structure. This allows us to easily identify $[O II] \lambda 3727$ emitters where often the $[O II] \lambda 3727$ doublet is the only emission feature. The spectra cover a wavelength range of approximately 4000 Å and were centered at an average wavelength of 7800 Å, although the exact wavelength range for each spectrum depends on the slit position with respect to the center of the mask along the dispersion direction. The G830 grating used with the OG550 blocker gives a throughput greater than 20% for most of this range and $\sim 28\%$ at 8150 Å. The observations were not generally taken at the parallactic angle, since this was determined by the mask orientation, so considerable care must be taken in measuring line fluxes as we discuss below. Each ~ 1 hr exposure was broken into three subsets, with the objects stepped along the slit by 1.5" in each direction. Some USELs were observed multiple times, resulting in total exposure times for these galaxies of 2–3 hr. The two-dimensional spectra were reduced following the procedure described in Cowie et al. (1996), and the final one-dimensional spectra were extracted using a profile weighting based on the strongest emission line in the spectrum. A small number of the spectra were obtained with the ZD600 line mm^{-1} grating, giving a correspondingly lower resolution but a wider wavelength coverage. These observations were centered at 7200 Å.

Essentially all of the emission-line candidates that were observed were identified, although two of the objects in the NB816 sample are stars where the absorption-line structure mimics emission in the band. Sample spectra are shown in Figures 3, 4, 5, and 6. The measured redshifts are given in Tables 2 and 3. The narrowband emission line selection produces a mixture of objects corresponding to $H\alpha$, $[O III] \lambda 5007$, and $[O II] \lambda 3727$ and, at the faintest magnitudes (>24), high-redshift $Ly\alpha$ emitters. The number of objects seen in each line and the redshifts where they are found are shown in Figure 7. The spectroscopically identified sample from both bands contains 13 $H\alpha$, 92 $[O III] \lambda 5007$, and 23 $[O II] \lambda 3727$ emitters. In the remainder of the paper we focus on the $H\alpha$ - and $[O III] \lambda 5007$ -selected galaxies that lie between redshifts zero and one.

Since only 30% of the USELs are spectroscopically identified, we must apply a substantial incompleteness correction in computing the line luminosity function and the universal star formation histories. Because the type mix may vary as a function of magnitude, we have adopted a magnitude-dependent weighting for each galaxy equal to the total number of galaxies at this magnitude divided by the number of spectroscopically identified galaxies. However, the analysis is not particularly sensitive to the adopted scheme since the fraction of identified galaxies is relatively constant with magnitude.

4. FLUX CALIBRATIONS

Generally our spectra were not obtained at the parallactic angle since this is determined by the DEIMOS mask orientation. Therefore, flux calibration using standard stars is problematic due to atmospheric refraction effects, and special care must be taken for the flux calibration. We therefore employed three independent methods for the flux calibration. In § 4.1 we define the “primary fluxes” of the emission lines used to select the galaxies. These primary fluxes are computed directly from the SuprimeCam broadband and narrowband magnitudes. We use these fluxes to derive the luminosity functions of $H\alpha$ and $[O III] \lambda 5007$ emitters at $z < 1$ (§ 5.1).

In § 4.2 we measure line fluxes from the spectra. Relative line fluxes can be measured from the spectra without flux calibration as long as we restrict the line measurements to short-wavelength ranges where the DEIMOS response is essentially constant. For example, one can assume that the responses of neighboring lines (e.g., $[O III] \lambda 4949$ and $[O III] \lambda 5007$) are the same, and therefore one can measure the flux ratio without calibration. For bright galaxies, we can absolutely calibrate the fluxes by integrating the spectra and equating them to the Subaru broadband fluxes. These line fluxes derived from the spectra are used as a check of the primary fluxes. We show that the ratio of $[O III] \lambda 5007/[O III] \lambda 4959$ is indeed close to 3 and that the fluxes computed from the spectra are highly consistent with the primary fluxes measured in § 4.1. In § 4.3 we show that Balmer flux ratios $f(H\beta)/f(H\alpha)$ of bright $H\alpha$ emitters are close to the case B conditions, suggesting very little reddening.

Metallicity measurements by the direct method require four emission lines that are widely displaced over the spectral wavelength range ($[O III] \lambda \lambda 4959, 5007, [O III] \lambda 4363$, and $[O II] \lambda 3727$). To calibrate these lines, we used neighboring Balmer lines with the assumption of case B conditions, and this is described in § 4.4.

4.1. Narrowband Fluxes: Primary Fluxes

For the emission lines used to select each galaxy we may compute the equivalent widths and absolute fluxes directly from the narrowband magnitudes (N) and the corresponding continuum

TABLE 2
NB816-SELECTED USEL SAMPLE

Number (1)	R.A. (J2000.0) (2)	Decl. (J2000.0) (3)	$N(AB)$ (4)	$z'(AB)$ (5)	I (6)	R (7)	V (8)	B (9)	z_{spec} (10)
1.....	40.115623	-1.694778	23.92	25.28	24.84	25.44	-99.00	-99.00	-1.0000
2.....	40.116665	-1.617472	24.26	25.88	25.52	25.74	-99.00	-99.00	-1.0000
3.....	40.138332	-1.405694	23.49	24.94	24.70	25.22	-99.00	-99.00	0.6343
4.....	40.174706	-1.704861	24.27	25.46	25.35	25.82	-99.00	-99.00	0.6355
5.....	40.183208	-1.495500	24.58	25.28	25.85	26.86	-99.00	-99.00	5.6886
6.....	40.217041	-1.494889	24.80	26.08	26.31	26.14	-99.00	-99.00	0.2416
7.....	40.250916	-1.744694	23.51	24.35	24.33	24.54	-99.00	-99.00	-1.0000
8.....	40.276291	-1.518222	24.72	24.78	25.53	25.75	-99.00	-99.00	-1.0000
9.....	40.276543	-1.623361	24.55	25.36	25.36	25.76	-99.00	-99.00	-1.0000
10.....	40.284168	-1.453667	21.82	23.20	23.02	22.56	-99.00	-99.00	0.2480
11.....	40.298878	-1.447472	24.32	25.95	25.42	25.71	-99.00	-99.00	-1.0000
12.....	40.304039	-1.391806	20.88	22.35	22.06	22.32	-99.00	-99.00	-1.0000
13.....	40.307045	-1.638611	24.91	25.67	25.72	26.02	-99.00	-99.00	-1.0000
14.....	40.311249	-1.535195	24.08	25.93	25.49	25.71	-99.00	-99.00	0.6240
15.....	40.318542	-1.548278	24.60	25.03	25.50	25.96	-99.00	-99.00	-1.0000
16.....	40.318832	-1.430972	23.37	23.77	24.32	24.42	-99.00	-99.00	1.1804
17.....	40.319122	-1.446417	23.60	23.85	24.43	24.56	-99.00	-99.00	1.1873
18.....	40.320793	-1.778083	20.70	21.57	21.60	21.86	-99.00	-99.00	-1.0000
19.....	40.324123	-1.410056	24.29	24.38	25.18	25.45	-99.00	-99.00	-1.0000
20.....	40.326042	-1.709833	23.24	24.75	24.62	24.96	-99.00	-99.00	-1.0000
21.....	40.336460	-1.570278	24.26	24.73	25.06	25.33	-99.00	-99.00	-1.0000
22.....	40.337292	-1.388278	24.81	27.37	26.71	26.77	-99.00	-99.00	-1.0000
23.....	40.337582	-1.658389	24.89	25.20	25.76	26.05	-99.00	-99.00	-1.0000
24.....	40.340378	-1.689500	24.55	26.37	26.07	26.51	-99.00	-99.00	-1.0000
25.....	40.340706	-1.551944	24.99	25.70	25.93	26.35	-99.00	-99.00	-1.0000
26.....	40.340874	-1.516333	24.89	25.06	25.69	25.78	-99.00	-99.00	-1.0000
27.....	40.340958	-1.371306	22.42	23.43	23.29	23.16	-99.00	-99.00	-1.0000
28.....	40.341331	-1.493583	23.37	24.62	24.55	24.23	-99.00	-99.00	-1.0000
29.....	40.341457	-1.484222	24.48	25.46	25.49	25.73	-99.00	-99.00	-1.0000
30.....	40.342918	-1.599611	24.65	25.31	25.50	25.85	-99.00	-99.00	-1.0000
31.....	40.343082	-1.438944	23.17	24.60	24.54	24.54	-99.00	-99.00	0.6226
32.....	40.347584	-1.403944	24.86	27.45	26.16	26.35	-99.00	-99.00	0.6324
33.....	40.349873	-1.598555	23.11	23.87	24.11	24.46	-99.00	-99.00	1.1956
34.....	40.356415	-1.515805	24.94	26.19	26.18	26.42	-99.00	-99.00	-1.0000
35.....	40.372250	-1.390472	23.85	24.68	24.72	24.62	-99.00	-99.00	-1.0000
36.....	40.373665	-1.722583	24.93	25.85	25.74	25.88	-99.00	-99.00	-1.0000
37.....	40.377918	-1.701972	23.45	23.82	24.26	24.70	-99.00	-99.00	-1.0000
38.....	40.388081	-1.697472	23.96	24.32	24.79	24.90	-99.00	-99.00	-1.0000
39.....	40.388916	-1.573472	24.79	25.13	25.65	26.07	-99.00	-99.00	-1.0000
40.....	40.394585	-1.521500	22.73	23.69	23.84	24.06	-99.00	-99.00	0.6291
41.....	40.395916	-1.374472	24.04	24.55	25.07	25.06	-99.00	-99.00	1.1811
42.....	40.395958	-1.507833	24.27	24.79	25.14	25.32	-99.00	-99.00	-1.0000
43.....	40.409168	-1.763222	24.34	24.86	25.22	25.23	-99.00	-99.00	-1.0000
44.....	40.416420	-1.728778	24.74	25.51	25.83	26.01	-99.00	-99.00	0.6192
45.....	40.437538	-1.651611	24.51	25.07	25.35	25.50	-99.00	-99.00	-1.0000
46.....	40.439831	-1.731944	24.77	25.38	25.70	25.62	-99.00	-99.00	-1.0000
47.....	40.441750	-1.466444	24.99	25.69	25.81	26.14	-99.00	-99.00	-1.0000
48.....	40.448750	-1.715833	23.72	25.28	24.83	25.10	-99.00	-99.00	-1.0000
49.....	40.450581	-1.457389	22.88	23.80	23.74	23.93	-99.00	-99.00	-1.0000
50.....	40.466961	-1.584972	24.38	25.40	25.20	25.32	-99.00	-99.00	-1.0000
51.....	40.472122	-1.524972	23.51	24.77	24.47	24.66	-99.00	-99.00	0.6359
52.....	40.480789	-1.686417	24.81	25.22	25.61	25.73	-99.00	-99.00	-1.0000
53.....	40.481750	-1.620750	23.80	24.56	24.78	25.25	-99.00	-99.00	-1.0000
54.....	40.484291	-1.714278	24.87	25.99	25.86	26.28	-99.00	-99.00	-1.0000
55.....	40.494457	-1.453583	24.97	25.57	25.94	26.06	-99.00	-99.00	-1.0000
56.....	40.503288	-1.533778	24.61	26.95	26.27	26.72	-99.00	-99.00	-1.0000
57.....	40.505081	-1.376083	22.05	23.38	22.91	23.28	-99.00	-99.00	-1.0000
58.....	40.514919	-1.504611	23.81	24.65	24.94	25.26	-99.00	-99.00	0.6238
59.....	40.520126	-1.523139	23.66	24.58	24.64	24.69	-99.00	-99.00	-2.0000
60.....	188.733032	62.057167	22.31	23.56	23.31	23.53	23.89	24.00	-1.0000
61.....	188.732742	62.349419	23.29	24.38	24.14	24.41	24.79	24.90	-1.0000
62.....	188.745621	62.164192	21.84	23.18	22.89	23.45	24.05	23.96	-1.0000
63.....	188.761505	62.410778	24.47	25.57	25.30	25.64	26.48	26.29	-1.0000
64.....	188.763535	62.287224	24.62	26.76	30.26	27.39	27.70	29.49	5.6985

TABLE 2—*Continued*

Number (1)	R.A. (J2000.0) (2)	Decl. (J2000.0) (3)	$N(AB)$ (4)	$z'(AB)$ (5)	I (6)	R (7)	V (8)	B (9)	z_{spec} (10)
65.....	188.769196	62.083973	24.72	24.85	25.69	25.58	27.06	32.17	−1.0000
66.....	188.778275	62.170082	24.68	25.31	25.58	25.70	26.57	26.11	−1.0000
67.....	188.828262	62.032722	22.40	23.49	23.32	23.52	24.12	24.28	−1.0000
68.....	188.868088	62.415138	24.72	25.55	25.53	26.05	26.60	26.10	−1.0000
69.....	188.873535	62.174362	22.58	24.08	23.75	23.99	24.39	24.44	−1.0000
70.....	188.885742	62.364082	24.10	26.07	25.22	25.92	26.33	26.40	0.6362
71.....	188.888214	62.057556	24.84	25.56	25.89	25.76	26.28	26.21	−1.0000
72.....	188.914429	62.247555	23.19	25.11	24.60	24.89	25.18	25.41	−1.0000
73.....	188.918243	62.020164	24.15	25.49	25.06	25.00	25.47	25.69	−1.0000
74.....	188.920532	62.105362	22.54	24.37	23.75	24.22	24.49	24.50	−1.0000
75.....	188.928421	62.127003	24.82	26.76	26.61	26.51	26.48	26.51	−1.0000
76.....	188.939423	62.334141	21.64	23.08	22.73	23.08	23.38	99.00	0.6319
77.....	188.943375	62.339664	23.49	24.66	24.75	24.87	25.35	25.56	−1.0000
78.....	188.950241	62.020889	23.84	25.73	25.39	26.02	26.80	26.28	−1.0000
79.....	188.954468	62.326195	24.68	26.01	25.55	25.92	26.58	26.58	−1.0000
80.....	188.957581	62.323471	23.45	24.71	24.41	24.67	25.12	25.08	−1.0000
81.....	188.964874	62.320164	23.45	24.82	24.41	24.81	24.97	25.20	0.6360
82.....	188.980362	62.104973	24.51	25.67	25.41	25.78	26.09	25.96	0.6426
83.....	188.985718	62.048695	24.23	24.87	25.03	24.89	25.76	25.62	0.6367
84.....	188.986221	62.341640	23.05	25.10	24.11	25.20	25.43	25.45	0.6352
85.....	188.991531	62.436169	24.91	24.25	26.03	25.28	24.90	27.58	−1.0000
86.....	188.992081	62.142998	24.49	25.50	25.47	25.57	26.30	26.18	0.6327
87.....	189.007919	61.996750	24.78	25.08	25.63	25.55	25.54	25.59	−1.0000
88.....	189.014206	62.362556	24.65	26.36	26.40	26.47	26.58	28.45	−1.0000
89.....	189.014877	62.359585	25.00	27.98	26.29	25.58	25.83	26.04	−1.0000
90.....	189.028870	62.145500	24.97	25.95	26.31	25.59	26.74	26.67	−1.0000
91.....	189.033127	61.994053	24.63	27.51	27.84	29.34	30.44	27.06	5.7138
92.....	189.039078	62.435024	24.65	25.13	25.49	24.95	25.34	25.46	−1.0000
93.....	189.045166	62.105392	23.80	25.58	25.08	25.37	26.06	25.92	−1.0000
94.....	189.056168	62.129974	24.88	26.25	26.27	30.24	26.85	29.17	5.6350
95.....	189.086044	62.195415	22.97	23.84	23.78	23.88	24.31	24.68	0.6297
96.....	189.090927	62.188831	24.57	24.45	25.47	26.76	28.00	27.57	5.4610
97.....	189.093658	61.999249	23.07	25.39	24.70	25.29	25.47	25.47	−1.0000
98.....	189.097824	62.272026	23.54	24.76	24.42	25.00	25.46	25.62	−1.0000
99.....	189.101456	62.395695	23.98	25.29	25.40	25.81	25.98	25.99	0.6322
100.....	189.106201	62.002777	23.64	25.00	24.81	25.11	25.44	25.51	−1.0000
101.....	189.110336	62.063030	24.96	26.25	26.25	27.16	28.02	27.85	5.7010
102.....	189.110916	62.245529	22.73	25.58	24.47	25.06	25.72	25.61	−1.0000
103.....	189.130417	62.038864	24.40	24.56	25.47	25.24	25.34	25.34	1.1952
104.....	189.138535	62.410442	24.83	24.99	25.68	25.16	27.97	27.37	−1.0000
105.....	189.176178	62.135834	24.58	25.22	25.57	25.39	26.14	26.38	−1.0000
106.....	189.190765	62.384472	24.34	25.91	25.98	25.60	25.72	26.05	0.2384
107.....	189.200897	62.328556	24.34	25.61	25.66	25.28	25.89	26.05	−1.0000
108.....	189.204910	62.192387	24.88	24.90	25.83	26.70	27.34	27.56	−1.0000
109.....	189.205292	62.013584	24.97	25.39	25.89	25.24	26.12	27.89	−1.0000
110.....	189.215210	62.326832	24.63	25.70	27.40	29.00	27.70	29.10	5.6750
111.....	189.216827	62.364609	24.84	29.07	27.06	27.32	27.78	28.67	5.6873
112.....	189.226837	62.394279	24.85	25.03	26.19	25.95	26.34	26.17	−1.0000
113.....	189.291046	62.367527	24.52	24.94	25.37	25.73	27.17	28.28	−1.0000
114.....	189.294052	62.055916	24.19	24.11	24.99	25.04	25.36	25.62	−1.0000
115.....	189.294083	62.035973	24.99	25.22	26.37	25.87	25.87	26.00	−1.0000
116.....	189.305740	62.340336	24.79	24.73	25.61	25.21	25.52	25.62	−1.0000
117.....	189.305542	62.421364	24.97	25.16	25.79	25.48	25.28	26.03	−1.0000
118.....	189.310959	62.174469	24.15	27.20	25.06	26.14	26.00	25.97	0.6439
119.....	189.313705	62.007584	24.79	28.49	25.86	26.45	26.57	26.81	−1.0000
120.....	189.360123	62.382584	24.51	25.01	25.62	25.37	25.68	25.66	−1.0000
121.....	189.361160	62.262306	24.26	25.78	25.44	25.76	26.67	26.62	0.0000
122.....	189.375626	62.392754	22.78	24.44	24.12	24.42	24.92	24.90	−1.0000
123.....	189.383194	62.286167	24.28	25.13	25.20	25.52	26.92	27.70	0.6342
124.....	189.383987	62.268448	24.96	25.12	29.03	25.78	26.47	26.10	−1.0000
125.....	189.383865	62.273277	24.72	25.09	25.55	25.01	26.05	26.11	−1.0000
126.....	189.387344	62.406555	23.85	26.55	25.59	26.42	27.56	27.19	−1.0000
127.....	189.390533	62.281364	24.69	26.82	26.21	25.28	25.17	25.06	−1.0000
128.....	189.391907	62.282108	24.77	29.34	26.91	25.30	26.53	26.36	−1.0000
129.....	189.392044	62.253914	24.02	29.56	25.53	26.03	26.17	26.58	−1.0000

TABLE 2—*Continued*

Number (1)	R.A. (J2000.0) (2)	Decl. (J2000.0) (3)	$N(AB)$ (4)	$z'(AB)$ (5)	I (6)	R (7)	V (8)	B (9)	z_{spec} (10)
130.....	189.408920	62.382164	24.82	25.24	25.64	25.84	25.70	25.93	−1.0000
131.....	189.436081	62.413029	24.18	24.61	25.29	25.48	25.71	25.78	−1.0000
132.....	189.436249	62.195915	24.90	27.54	26.96	26.51	27.56	27.35	5.6699
133.....	189.438965	62.223331	24.59	24.51	25.40	26.46	27.28	28.82	−1.0000
134.....	189.461365	62.147663	23.51	25.79	24.88	25.33	25.92	26.21	0.0000
135.....	189.497375	62.344833	24.74	25.28	25.60	25.63	25.99	25.42	−1.0000
136.....	189.508835	62.273308	24.36	24.79	25.41	25.37	25.75	25.88	−1.0000
137.....	189.514969	62.243473	22.39	23.57	23.56	23.93	23.93	24.12	1.1802
138.....	189.517288	62.246944	23.30	23.95	24.15	24.31	24.30	24.45	−1.0000
139.....	189.518616	62.384193	24.45	24.71	25.33	25.26	25.50	25.52	−1.0000
140.....	189.533279	62.349331	22.29	22.88	23.10	23.48	23.64	23.72	−1.0000
141.....	189.537338	62.413666	24.96	27.71	27.55	26.36	29.18	26.44	−1.0000
142.....	189.552673	62.398167	23.68	24.20	24.62	24.81	24.84	24.86	−1.0000
143.....	189.566376	62.396610	24.87	25.87	26.50	26.31	25.91	25.88	−1.0000
144.....	189.570587	62.057972	24.50	24.81	25.36	25.52	26.43	26.00	−1.0000
145.....	189.577286	62.272663	24.81	26.26	29.31	27.10	28.23	27.21	5.7275
146.....	189.600052	62.202751	24.94	25.64	25.95	25.24	25.63	26.24	−1.0000
147.....	189.607834	62.433750	24.72	25.87	25.53	26.00	29.06	27.20	−1.0000
148.....	189.608383	62.387306	23.96	24.27	24.90	25.08	25.20	25.23	0.0000
149.....	189.612579	62.207664	24.12	24.25	25.00	25.54	27.38	27.19	0.0000
150.....	189.629166	62.255390	23.04	23.56	23.87	24.15	24.25	24.29	1.1843
151.....	189.635117	62.404610	24.94	24.99	25.79	25.79	26.24	26.43	−1.0000
152.....	189.638306	62.205860	24.76	24.51	25.59	28.85	26.53	27.55	0.0000
153.....	189.653839	62.249142	23.94	24.23	25.00	25.09	25.10	25.40	−1.0000
154.....	189.654907	62.099976	24.14	25.59	25.26	25.57	26.36	27.11	0.0000
155.....	189.677246	62.143169	24.91	24.30	25.73	28.55	27.49	27.64	−1.0000
156.....	189.680618	62.392223	24.63	25.31	25.46	24.90	25.57	25.80	−1.0000
157.....	334.191620	0.370306	23.79	25.71	24.79	25.64	25.86	26.22	−1.0000
158.....	334.195343	0.162833	23.73	23.93	24.58	25.22	25.51	25.63	1.1911
159.....	334.198517	0.264389	24.99	25.11	25.88	26.42	30.98	25.40	−1.0000
160.....	334.208710	0.263056	24.92	25.21	25.80	25.42	24.97	24.86	−1.0000
161.....	334.212219	0.440861	22.47	23.45	23.35	23.83	24.35	24.22	−1.0000
162.....	334.210144	0.341056	24.95	25.55	25.88	26.14	26.29	26.45	−1.0000
163.....	334.217438	0.413917	23.85	25.70	24.97	25.69	26.93	25.94	−1.0000
164.....	334.216248	0.101194	22.52	24.19	23.61	24.43	24.85	24.83	−1.0000
165.....	334.219299	0.225444	22.67	24.41	23.94	24.65	25.13	24.96	−1.0000
166.....	334.222290	0.093000	22.97	23.39	23.81	24.46	24.68	24.76	1.1845
167.....	334.223785	0.307833	24.92	25.04	25.75	26.34	26.23	26.45	0.0000
168.....	334.225037	0.248528	24.35	25.08	25.19	25.23	26.37	26.63	−1.0000
169.....	334.228882	0.094083	23.93	26.55	26.09	99.00	99.00	27.71	5.6765
170.....	334.228577	0.454000	22.74	24.46	23.98	24.87	25.43	25.71	−1.0000
171.....	334.233612	0.411389	24.67	24.82	25.54	26.02	25.87	25.88	−1.0000
172.....	334.246246	0.387722	23.37	25.51	24.65	25.50	25.84	25.73	0.6177
173.....	334.265045	0.086528	24.47	25.56	25.57	26.34	26.23	26.67	−1.0000
174.....	334.266937	0.086083	24.98	25.28	25.85	26.64	25.68	26.44	0.0000
175.....	334.273193	0.216889	24.41	25.85	26.14	99.00	99.00	29.49	5.6703
176.....	334.275391	0.397806	22.32	23.07	23.36	24.17	24.60	24.63	−1.0000
177.....	334.283051	0.060000	24.92	25.46	25.76	26.04	27.99	25.84	−1.0000
178.....	334.290039	0.054444	24.04	24.85	24.84	25.10	99.00	25.29	0.6210
179.....	334.302704	0.252750	24.32	24.76	25.13	25.64	25.77	25.58	0.0000
180.....	334.336914	0.335333	24.55	27.03	26.26	27.85	27.07	27.21	5.6706
181.....	334.337219	0.293806	24.10	24.83	25.65	99.00	99.00	99.00	5.6672
182.....	334.343658	0.078083	23.06	24.24	24.03	24.55	24.88	24.77	−1.0000
183.....	334.346863	0.317306	24.79	25.21	25.61	25.96	25.85	25.70	1.1919
184.....	334.346741	0.316694	22.57	23.12	23.38	23.92	24.11	23.88	1.1919
185.....	334.351868	0.197222	24.72	27.39	27.92	28.47	26.94	99.00	0.0000
186.....	334.359161	0.253528	24.04	26.85	25.47	26.73	29.17	27.79	0.6167
187.....	334.360413	0.466722	24.81	25.32	25.94	26.50	28.69	27.92	−1.0000
188.....	334.369751	0.321694	24.29	25.08	25.29	27.11	28.39	28.26	5.6416
189.....	334.373138	0.344361	24.98	99.00	27.50	26.29	27.72	27.87	−1.0000
190.....	334.373199	0.300861	23.93	24.26	24.75	25.23	25.59	25.10	1.1866
191.....	334.381714	0.160278	24.59	25.99	26.55	28.61	99.00	27.96	5.6840
192.....	334.383118	0.344750	24.94	26.88	27.24	27.20	27.18	99.00	−1.0000
193.....	334.387909	0.371278	24.36	26.17	25.95	28.08	26.66	99.00	5.6531
194.....	334.390808	0.450500	24.19	25.74	25.40	26.03	26.52	25.76	−1.0000

TABLE 2—*Continued*

Number (1)	R.A. (J2000.0) (2)	Decl. (J2000.0) (3)	<i>N</i> (AB) (4)	<i>z'</i> (AB) (5)	<i>I</i> (6)	<i>R</i> (7)	<i>V</i> (8)	<i>B</i> (9)	<i>z</i> _{spec} (10)
195.....	334.404327	0.377528	22.59	23.77	23.49	24.05	24.55	24.57	0.6286
196.....	334.416016	0.307361	24.86	26.68	26.49	28.45	28.16	26.76	5.7240
197.....	334.420380	0.404250	24.93	25.77	25.76	28.87	27.81	99.00	5.6330
198.....	334.418121	0.667972	23.43	25.00	24.85	25.20	25.74	25.87	0.6267
199.....	334.426331	0.128833	24.44	24.96	26.15	99.00	28.33	99.00	0.0000
200.....	334.428894	0.225694	22.87	25.09	24.39	24.96	25.44	25.02	0.6270
201.....	334.430969	0.219639	24.73	26.16	25.74	26.05	27.01	26.83	0.6269
202.....	334.433289	0.225944	22.91	23.82	23.73	24.14	24.64	24.24	0.6278
203.....	334.439117	0.471750	23.06	24.29	23.86	24.41	24.95	24.69	0.6175
204.....	334.441345	0.053583	24.41	24.48	25.23	25.38	25.27	25.43	1.1832
205.....	334.444305	0.374917	23.15	24.49	24.24	24.79	25.38	25.31	−1.0000
206.....	334.443848	0.657750	23.00	27.31	25.07	26.02	26.59	26.20	0.6276
207.....	334.445251	0.237194	24.39	26.76	26.02	26.36	26.33	26.31	−1.0000
208.....	334.449829	0.253722	22.59	25.66	24.49	25.62	26.36	25.81	0.6263
209.....	334.457672	0.396028	23.27	25.17	24.61	25.53	25.83	25.74	−1.0000
210.....	334.474579	0.741528	24.82	25.56	25.79	25.55	25.51	25.49	−1.0000
211.....	334.479889	0.485722	24.43	25.52	25.95	27.58	101.9	31.94	5.7265
212.....	334.484650	0.273250	23.73	26.26	25.06	26.41	26.59	26.44	0.6247
213.....	334.490356	0.825528	24.59	26.02	25.56	26.09	26.37	26.56	0.6406
214.....	334.502625	0.340917	24.30	25.68	25.20	25.53	26.14	26.44	−1.0000
215.....	334.509094	0.242111	24.12	25.92	25.99	99.00	99.00	99.00	5.6738
216.....	334.513123	0.088639	21.34	22.68	22.43	22.40	23.16	23.00	−1.0000
217.....	334.515167	0.367639	24.24	26.31	25.40	25.97	25.98	26.28	−1.0000
218.....	334.518890	0.239472	24.81	27.43	28.70	99.00	99.00	99.00	5.6807
219.....	334.533783	0.676139	24.60	25.01	25.49	25.75	25.66	25.58	−1.0000
220.....	334.535431	0.110722	24.96	25.93	26.53	26.96	27.67	26.77	−1.0000
221.....	334.543335	0.117583	23.98	25.92	25.58	26.53	27.14	27.22	0.6216
222.....	334.543884	0.254056	24.62	25.41	25.55	26.13	26.73	26.52	−1.0000
223.....	334.546783	0.183778	23.16	24.63	24.36	24.92	25.69	25.14	0.6288
224.....	334.550323	0.420528	24.01	24.66	24.85	25.27	25.29	24.84	1.1865
225.....	334.554443	0.442000	24.94	25.50	25.86	26.00	26.11	25.38	−1.0000
226.....	334.555389	0.198833	24.29	27.20	25.94	26.66	26.98	27.71	−1.0000
227.....	334.556976	0.454917	23.59	24.05	24.46	24.95	24.93	24.79	1.1877
228.....	334.557159	0.106000	24.94	25.78	25.78	26.31	26.23	26.51	−1.0000
229.....	334.562775	0.664444	23.68	24.09	24.51	24.57	24.68	26.65	−1.0000
230.....	334.565613	0.105222	24.01	26.53	24.89	25.67	25.69	25.86	−1.0000
231.....	334.569214	0.432139	22.62	23.21	23.44	24.01	24.37	24.15	−1.0000
232.....	334.576172	0.398639	23.23	24.10	24.35	25.21	25.45	25.68	1.1858
233.....	334.577118	0.454083	24.77	25.61	25.99	26.23	26.93	26.46	−1.0000
234.....	334.581390	0.359000	24.43	24.74	25.26	25.75	26.29	25.88	−1.0000
235.....	334.582886	0.130917	23.25	24.48	24.15	24.94	25.40	25.14	−1.0000
236.....	334.589722	0.794278	24.88	25.14	25.68	25.83	26.35	26.68	1.1731
237.....	334.593781	0.468806	24.69	25.66	26.06	26.29	25.95	26.59	−1.0000
238.....	334.597961	0.159111	23.73	25.87	25.05	25.24	26.46	26.07	−1.0000
239.....	334.597015	0.422083	23.89	25.69	25.11	25.81	26.15	26.02	−1.0000
240.....	334.602356	0.346472	24.96	25.85	25.95	27.89	99.00	28.00	−1.0000
241.....	334.606415	0.159028	23.68	25.80	25.08	25.70	27.01	26.85	−1.0000
242.....	334.607574	0.728944	24.63	26.30	25.73	25.54	25.98	26.06	0.0000
243.....	334.636139	0.479083	24.32	25.90	25.83	27.58	29.70	27.44	5.6820
244.....	334.641937	0.466944	24.52	25.39	25.48	25.66	26.18	26.37	0.6255
245.....	334.641449	0.610944	24.90	25.17	26.17	28.82	101.9	101.63	0.0000
246.....	334.654999	0.586889	24.54	25.82	25.49	25.22	25.82	25.68	−1.0000
247.....	334.679749	0.744222	24.80	26.48	26.57	102.18	101.99	101.63	5.6560
248.....	334.682465	0.455139	24.73	25.32	25.71	25.36	26.07	26.89	−1.0000
249.....	334.689270	0.717278	23.36	24.60	24.51	24.62	25.29	25.47	−1.0000
250.....	334.689270	0.717278	22.90	23.98	23.80	23.91	24.56	24.56	−1.0000
251.....	334.692444	0.556167	24.66	24.47	25.62	25.66	26.00	25.84	−1.0000
252.....	334.714386	0.711056	22.47	23.86	23.36	23.67	24.11	24.15	0.6414
253.....	334.715454	0.731028	24.20	26.01	25.33	26.10	26.68	26.57	0.6413
254.....	334.723999	0.540750	23.02	25.18	24.51	24.98	25.39	25.73	0.6230
255.....	334.727081	0.528639	24.10	25.23	25.00	25.32	25.83	26.10	−1.0000
256.....	334.727264	0.455472	24.36	25.18	25.51	26.28	26.39	26.20	0.0000
257.....	334.735687	0.561056	22.04	21.09	23.38	22.16	21.87	22.49	−2.0000
258.....	334.759155	0.586722	23.18	23.11	24.14	23.63	24.25	25.11	0.6453
259.....	334.770844	0.514667	24.88	101.71	27.94	31.27	101.99	30.28	5.6960

TABLE 2—*Continued*

Number (1)	R.A. (J2000.0) (2)	Decl. (J2000.0) (3)	$N(AB)$ (4)	$z'(AB)$ (5)	I (6)	R (7)	V (8)	B (9)	z_{spec} (10)
260.....	334.776031	0.517750	24.89	24.82	25.74	26.87	27.96	25.66	−1.0000
261.....	334.778687	0.517583	24.45	24.28	25.25	25.43	25.89	25.34	−1.0000
262.....	334.788330	0.628972	24.97	25.57	25.91	25.88	101.9	26.37	−1.0000
263.....	334.788818	0.769639	23.16	24.04	24.05	24.08	24.46	24.73	0.2430
264.....	334.788116	0.589528	21.57	21.04	22.80	21.68	21.64	21.10	−1.0000
265.....	334.792511	0.593722	23.97	26.50	25.02	25.87	25.71	25.92	−1.0000
266.....	334.793549	0.602611	24.49	25.26	25.32	25.64	25.71	26.30	−1.0000
267.....	334.796783	0.489083	24.70	25.26	25.55	25.74	26.00	26.12	−1.0000

NOTES.—Magnitudes are measured in $3''$ diameter apertures. An entry of “−99” indicates that no excess flux was measured, while “99” means that there was a negative flux in the aperture. A value of −1.0000 in the redshift column means that no spectroscopic data were obtained for the object, 0.0000 means that spectra were obtained, but the object was not identified, while −2.0000 denotes a star.

magnitudes (C) from our SuprimeCam imaging data. For example, in the case of the NB816-selected emission-line galaxies, N corresponds to the NB816 magnitude and C is the I -band magnitude. We refer to the values calculated in this way as the “primary fluxes” and use this quantity to compute the luminosity functions for each emitter in § 5.1.

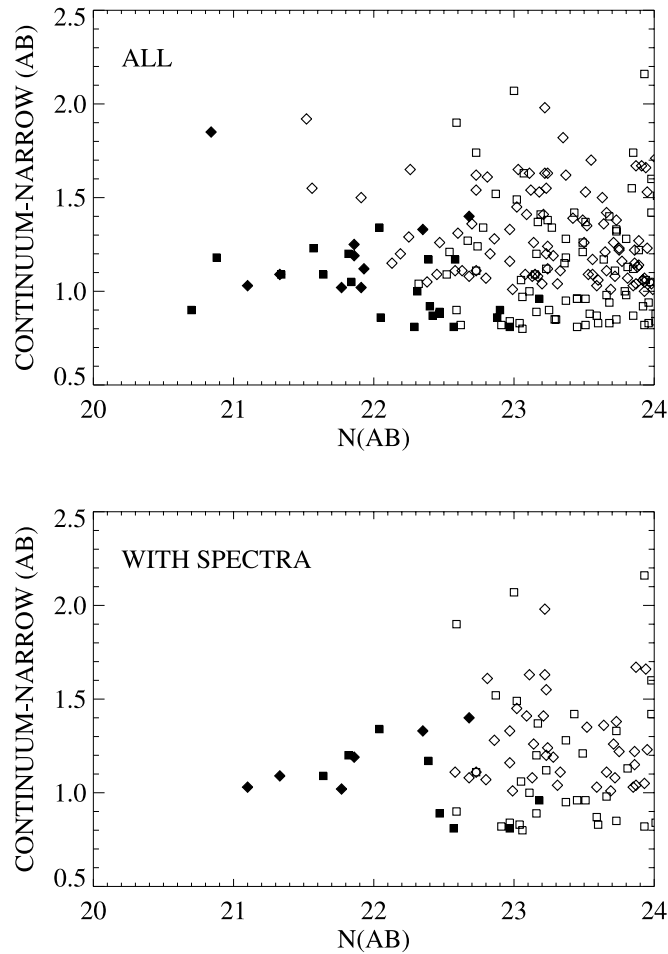


FIG. 2.—Continuum narrowband magnitude vs. narrowband magnitude for all objects with narrowband magnitude brighter than 24. The diamonds show the narrowband excess emission magnitude of the NB912 sample, and the squares the NB816 sample. Galaxies that would be included in an $R < 24$ continuum-selected sample are shown with filled symbols. The top panel shows the complete sample, while the bottom panel shows the subsample that has been spectroscopically identified.

Defining the quantity

$$R = 10^{-0.4(N-C)},$$

the observed-frame equivalent width becomes

$$EW = R - 1\phi - \frac{R}{\Delta\lambda},$$

where ϕ is the narrowband filter response normalized such that the integral over wavelength is unity and $\Delta\lambda$ is the effective width of the continuum filter. The narrowband filter is often assumed to be rectangular, in which case ϕ becomes $1/\delta\lambda$, where $\delta\lambda$ is the width of the narrow band, but as can be seen from Figure 1, this is not a very good approximation in the present case. For very high equivalent width objects the denominator in this equation becomes uncertain unless the broadband data are very deep, and this can result in a large scatter in the very highest equivalent widths where the continuum is poorly determined.

In the case of the $[O\text{ III}]\lambda 5007$ line we must include the second member of the doublet, which also lies within the narrowband filter. We have computed these cases assuming that the flux of the $[O\text{ III}]\lambda 4959$ line is 0.34 times that of the $[O\text{ III}]\lambda 5007$ line. Then $\phi = \phi_1 + 0.34\phi_2$, where ϕ_1 is the filter response at the redshifted 5007 Å wavelength and ϕ_2 is the filter response at redshifted 4959 Å.

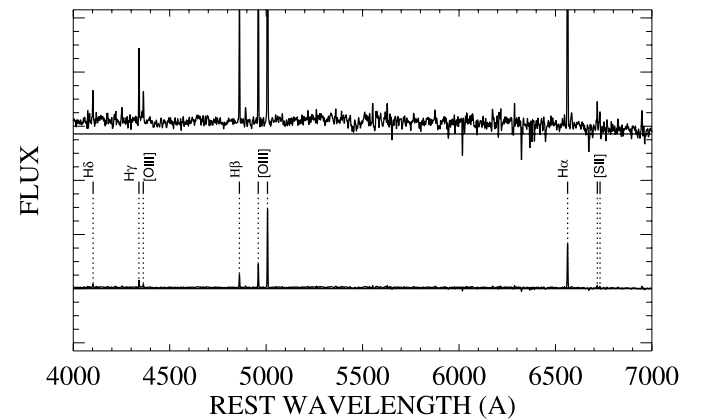


FIG. 3.—Spectrum of an $H\alpha$ emission galaxy selected in the NB912 filter. In the top panel we have decreased the scale of the vertical axis by a factor of 10 to show the continuum and the weaker lines. The more important emission-line features are labeled and marked with the dotted lines.

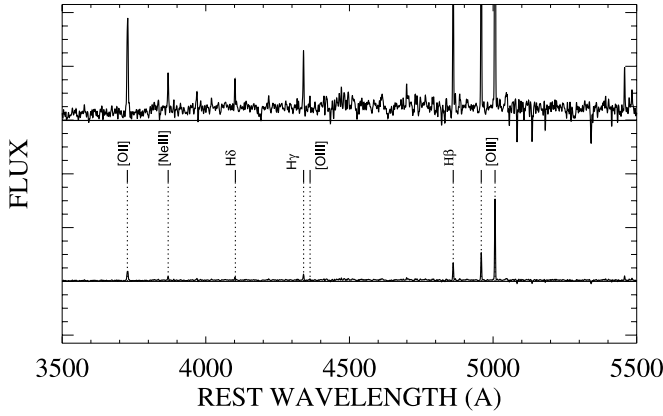


FIG. 4.—Spectrum of an [O III] galaxy in the NB816-selected sample. The bottom panel shows the relative strengths of the very strong emission lines in the spectrum. In the top panel we have decreased the scale of the vertical axis by a factor of 10 to show the continuum and the weaker lines. The more important emission-line features are labeled and marked with the dotted lines.

The distribution of the rest-frame equivalent widths for the H α and [O III] λ 5007 samples is shown in Figure 8. The [O III] λ 5007 sample selects objects with rest-frame equivalent widths above about 100 Å, while the lower redshift H α sample selects objects with rest-frame equivalent widths above about 150 Å. Since the [O III] λ 5007 lines are also generally stronger than the H α lines, the [O III] selection chooses less extreme objects than the H α selection and will include a larger fraction of galaxies at the given redshift.

The high observed-frame equivalent widths make the line fluxes insensitive to the continuum determination, and these may simply be found from

$$f = A \left(\frac{10^{-0.4N} - 10^{-0.4C}}{\phi - 1/\Delta\lambda} \right),$$

where A is the AB zero point at the narrowband wavelength in units of $\text{ergs cm}^{-2} \text{s}^{-1} \text{Å}^{-1}$. The flux depends on the filter response at the emission-line wavelength and correspondingly is most uncertain at the edges of the filters where this quantity changes rapidly. Primary fluxes defined here are measured by using narrowband (N) and broadband (C) magnitudes from Subaru imaging data with the object redshift information from Keck spectra for

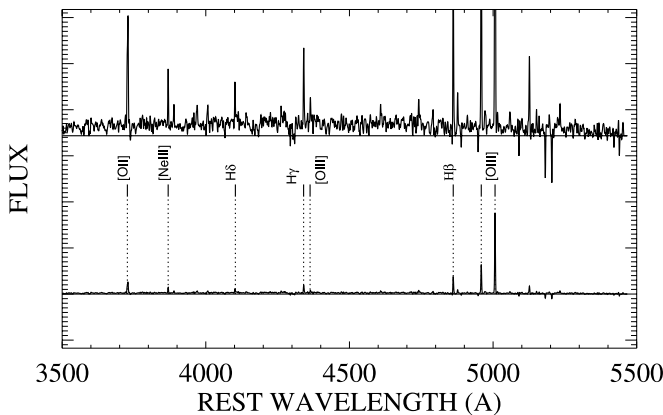


FIG. 5.—Spectrum of an [O III] galaxy selected in the NB912 filter. The bottom panel shows the relative strengths of the very strong emission lines in the spectrum. In the top panel we have decreased the scale of the vertical axis by a factor of 10 to show the continuum and the weaker lines. The more important emission-line features are labeled and marked with the dotted lines.

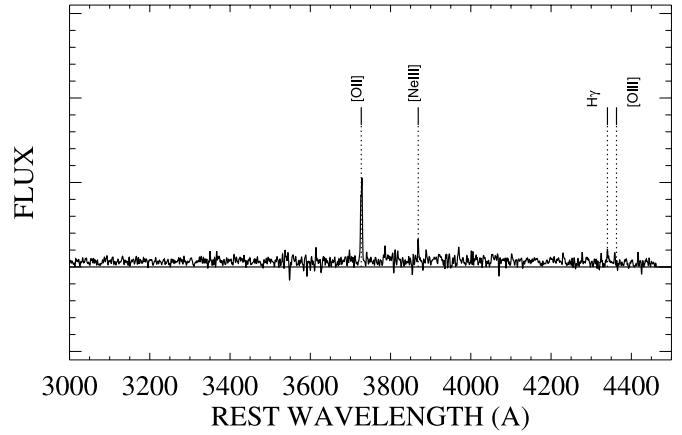


FIG. 6.—Spectrum of an [O II] galaxy selected in the NB816 filter. The plot shows the relative strengths of the very strong emission lines in the spectrum. The more important emission-line features are labeled and marked with the dotted lines.

the filter response at the exact location of emission-line wavelength (ϕ). We use these primary fluxes to construct the luminosity functions of H α - and [O III] λ 5007–selected emitters as we discuss in § 5.1.

4.2. Line Fluxes from the Spectra

For the short-wavelength range where DEIMOS response is essentially constant, we may also compute the relative line fluxes from the spectra without calibration. For each spectrum we fitted a standard set of lines. For the stronger lines we used a full Gaussian fit together with a linear fit to the continuum baseline. For weaker lines we held the full width constant using the value measured in the stronger lines and set the central wavelength to the nominal redshifted value. We also measured the noise as a function of wavelength by fitting to random positions in the spectrum and computing the dispersion in the results.

In follow-up work to the present analysis we have obtained much deeper spectra for several of the objects. Up to 6 hr of data have been obtained in the form of multiple 1 hr exposures with DEIMOS on Keck. The discussion of these data will be given in L. L. Cowie et al. (2007, in preparation). We have used these data to test the noise analysis in the individual spectra by comparing this noise with the dispersion among the line flux measurements in each of the individual spectra comprising the multiple observations. The two methods give consistent determinations for the noise, and in all cases the newer measurements of the line strengths in the combined deeper spectra are fully consistent with the present observations although with much smaller error bars.

These fits should provide accurate relative fluxes over short-wavelength intervals where the DEIMOS response is similar but may be expected to be poorer over longer wavelength intervals where the true calibration can vary from the adopted value. We tested the relative flux calibration for neighboring lines and the noise measurement by measuring the ratio of the [O III] λ 4959/[O III] λ 5007 lines. This is expected to have a value of approximately 0.34. The ratio is shown as a function of the [O III] λ 5007 flux in Figure 9. The measured values scatter around the expected value and the dispersion is consistent with the noise determination. This result supports our assumption of [O III] λ 4959/[O III] λ 5007 = 0.34 in the primary flux measurements described in § 4.1. However, a small upward trend can be seen in the ratio as we move toward weaker fluxes. This is a consequence of the full Gaussian fits overestimating the strength of weak lines and is the

TABLE 3
NB912-SELECTED USEL SAMPLE

Number (1)	R.A. (J2000.0) (2)	Decl. (J2000.0) (3)	$N(\text{AB})$ (4)	$z'(\text{AB})$ (5)	I (6)	R (7)	V (8)	B (9)	z_{spec} (10)
1.....	40.131710	-1.408361	23.86	25.08	25.89	25.97	-99.00	-99.00	0.8371
2.....	40.133957	-1.575250	24.76	25.92	26.13	25.84	-99.00	-99.00	1.4498
3.....	40.148125	-1.593611	23.21	24.62	25.53	26.11	-99.00	-99.00	0.8206
4.....	40.148376	-1.725417	24.76	25.97	26.98	26.39	-99.00	-99.00	0.8111
5.....	40.150795	-1.737583	23.31	24.35	24.88	25.32	-99.00	-99.00	0.8269
6.....	40.153290	-1.536833	23.64	25.00	26.18	26.87	-99.00	-99.00	0.8301
7.....	40.156544	-1.765833	21.93	23.05	23.51	23.74	-99.00	-99.00	-1.0000
8.....	40.165752	-1.580139	24.94	26.20	25.92	25.84	-99.00	-99.00	1.4482
9.....	40.183250	-1.389611	21.77	22.79	23.33	23.52	-99.00	-99.00	0.8325
10.....	40.184338	-1.596472	23.09	24.50	25.30	25.55	-99.00	-99.00	0.8291
11.....	40.193504	-1.690111	24.32	25.40	25.83	25.69	-99.00	-99.00	0.8266
12.....	40.194084	-1.373750	23.93	24.93	25.21	25.35	-99.00	-99.00	-1.0000
13.....	40.194710	-1.373917	24.87	25.90	26.30	26.47	-99.00	-99.00	-1.0000
14.....	40.196709	-1.378389	24.07	25.42	26.05	26.18	-99.00	-99.00	-1.0000
15.....	40.202122	-1.584472	24.22	25.30	25.81	26.19	-99.00	-99.00	0.8289
16.....	40.203335	-1.471861	24.77	26.20	25.78	25.54	-99.00	-99.00	0.3965
17.....	40.214748	-1.519944	23.14	24.40	25.38	25.94	-99.00	-99.00	0.8289
18.....	40.220333	-1.753778	24.34	25.41	26.40	26.29	-99.00	-99.00	-1.0000
19.....	40.220997	-1.388611	23.24	24.36	25.13	24.99	-99.00	-99.00	-1.0000
20.....	40.226917	-1.542139	23.02	24.47	25.77	25.48	-99.00	-99.00	0.8209
21.....	40.229126	-1.720944	24.99	27.85	27.11	102.70	-99.00	-99.00	6.4800
22.....	40.229332	-1.376472	23.75	24.98	25.72	24.66	-99.00	-99.00	-1.0000
23.....	40.245834	-1.578972	24.61	25.82	27.22	26.91	-99.00	-99.00	0.8285
24.....	40.280624	-1.421111	24.82	25.86	26.13	25.91	-99.00	-99.00	-1.0000
25.....	40.290958	-1.746389	23.89	25.16	25.81	25.03	-99.00	-99.00	0.0000
26.....	40.323959	-1.697695	24.73	25.80	26.47	25.71	-99.00	-99.00	-1.0000
27.....	40.330791	-1.612417	23.03	24.68	26.06	25.47	-99.00	-99.00	0.0000
28.....	40.339832	-1.395361	23.87	25.54	26.98	25.45	-99.00	-99.00	0.3887
29.....	40.346794	-1.448389	23.93	24.98	25.37	25.48	-99.00	-99.00	0.8274
30.....	40.382538	-1.554111	23.52	24.87	25.60	25.08	-99.00	-99.00	0.3930
31.....	40.393124	-1.713750	24.94	26.83	26.70	26.50	-99.00	-99.00	-1.0000
32.....	40.398834	-1.466583	23.87	24.91	24.83	24.64	-99.00	-99.00	1.4590
33.....	40.403870	-1.530195	24.88	26.08	27.44	27.30	-99.00	-99.00	0.8223
34.....	40.409500	-1.369278	21.52	23.44	24.47	24.04	-99.00	-99.00	-1.0000
35.....	40.411705	-1.691445	24.41	25.50	25.68	25.55	-99.00	-99.00	-1.0000
36.....	40.425083	-1.454111	21.91	22.93	23.42	23.41	-99.00	-99.00	-1.0000
37.....	40.429913	-1.501139	23.13	24.21	24.76	24.92	-99.00	-99.00	0.8267
38.....	40.446251	-1.676111	24.91	26.09	26.37	26.04	-99.00	-99.00	-1.0000
39.....	40.479042	-1.534250	24.87	26.06	25.79	25.56	-99.00	-99.00	0.3861
40.....	40.506042	-1.755111	22.73	24.27	25.24	25.19	-99.00	-99.00	-1.0000
41.....	40.511585	-1.597000	24.73	25.96	25.55	25.67	-99.00	-99.00	-1.0000
42.....	40.518124	-1.666167	22.47	23.73	24.37	24.45	-99.00	-99.00	-1.0000
43.....	188.802414	62.319778	24.91	26.26	26.19	26.10	26.43	22.53	-1.0000
44.....	188.805588	62.377583	24.47	25.51	25.60	25.66	26.37	22.13	-1.0000
45.....	188.809082	62.093307	24.71	26.06	25.59	25.18	25.33	21.60	-1.0000
46.....	188.817169	62.153473	24.91	26.46	27.75	28.42	28.59	23.85	-1.0000
47.....	188.833542	62.108307	25.00	26.27	25.08	25.84	25.92	22.33	-1.0000
48.....	188.837997	62.134029	24.90	26.87	27.82	27.49	28.70	24.06	-1.0000
49.....	188.841248	62.123669	24.69	25.81	25.92	26.62	26.48	23.59	-1.0000
50.....	188.856094	62.064747	22.73	24.35	25.13	25.14	25.56	21.75	-1.0000
51.....	188.892212	62.181778	24.42	25.43	25.47	25.02	25.46	21.41	-1.0000
52.....	188.919495	62.299862	21.33	22.42	22.78	22.36	22.68	19.17	0.3960
53.....	188.919373	62.255695	24.93	26.30	26.48	26.25	26.55	22.17	-1.0000
54.....	188.936844	62.081692	24.89	26.44	27.05	27.14	27.74	23.53	-1.0000
55.....	188.939911	62.118752	24.97	26.50	25.54	26.18	26.56	22.60	-1.0000
56.....	188.949173	62.062248	21.86	23.11	23.70	23.56	23.85	19.91	-1.0000
57.....	188.955826	62.066334	24.94	26.04	25.63	25.87	26.38	22.69	-1.0000
58.....	188.972321	62.191444	24.10	25.32	25.41	24.94	25.51	21.91	-1.0000
59.....	188.978271	62.142639	24.87	26.22	26.43	26.04	26.11	22.09	-1.0000
60.....	189.024841	62.289722	23.23	24.43	24.72	24.43	25.06	21.51	0.3898
61.....	189.027618	62.082359	24.45	26.22	26.13	29.43	28.12	22.90	-1.0000
62.....	189.046036	62.360138	24.90	26.33	25.91	26.63	28.17	23.34	-1.0000
63.....	189.047668	62.101501	24.59	26.06	25.91	25.99	26.15	22.47	-1.0000
64.....	189.057831	62.172222	24.85	26.29	29.31	25.95	26.99	22.85	-1.0000

TABLE 3—*Continued*

Number (1)	R.A. (J2000.0) (2)	Decl. (J2000.0) (3)	$N(AB)$ (4)	$z'(AB)$ (5)	I (6)	R (7)	V (8)	B (9)	z_{spec} (10)
65.....	189.074799	62.157028	24.79	25.82	25.19	25.29	25.70	21.66	−1.0000
66.....	189.082825	62.139248	24.90	26.07	25.56	25.76	26.25	22.06	−1.0000
67.....	189.119370	62.362720	23.89	25.03	25.16	25.54	25.49	21.44	−1.0000
68.....	189.125137	62.034111	24.73	26.52	26.33	27.12	34.42	23.51	0.0000
69.....	189.154999	62.188332	24.22	25.41	25.74	25.68	25.80	21.65	0.8396
70.....	189.164536	62.283306	24.70	25.71	25.25	25.91	26.45	22.79	−1.0000
71.....	189.172470	62.179943	24.97	26.39	26.86	26.65	26.68	22.95	−1.0000
72.....	189.189438	62.313778	24.81	26.13	26.08	26.32	26.69	24.03	−1.0000
73.....	189.202087	62.189083	24.65	26.36	29.91	27.17	29.50	24.18	−1.0000
74.....	189.206757	62.203587	24.71	25.83	25.59	25.32	25.19	21.30	−1.0000
75.....	189.219162	62.161583	24.98	26.04	25.14	25.05	24.90	21.11	−1.0000
76.....	189.226044	62.342197	23.92	24.98	25.30	25.83	25.89	22.21	−1.0000
77.....	189.278076	62.402336	24.59	27.20	27.42	26.50	29.04	26.79	−1.0000
78.....	189.296036	62.053169	24.38	25.53	26.06	26.50	26.94	22.63	0.0000
79.....	189.296417	62.052696	23.65	24.86	26.14	25.88	26.17	22.09	0.0000
80.....	189.304382	62.258610	23.50	24.76	25.63	25.46	25.56	21.82	−1.0000
81.....	189.308090	62.118610	22.83	24.03	24.81	24.72	25.01	21.20	−1.0000
82.....	189.312881	62.284142	24.89	26.61	26.56	27.01	26.91	23.12	−1.0000
83.....	189.314819	62.364780	24.90	26.42	25.84	25.73	25.70	21.80	−1.0000
84.....	189.317169	62.388390	24.55	25.70	26.04	25.70	26.06	21.99	−1.0000
85.....	189.346817	62.067139	22.97	24.30	24.82	24.98	25.04	21.19	0.8280
86.....	189.354828	62.390472	24.88	26.28	27.87	26.58	27.14	24.22	−1.0000
87.....	189.387344	62.265694	25.00	26.85	26.02	25.45	25.46	21.90	−1.0000
88.....	189.391907	62.387859	24.85	26.71	27.44	27.55	26.43	23.56	−1.0000
89.....	189.400620	62.083500	24.91	26.89	27.89	26.19	26.65	23.79	−1.0000
90.....	189.401199	62.214943	24.49	25.53	25.83	25.78	25.75	22.08	−1.0000
91.....	189.404999	62.102139	24.24	25.28	25.49	25.41	25.23	21.28	−1.0000
92.....	189.421585	62.397167	24.98	26.10	25.63	25.59	25.84	21.68	−1.0000
93.....	189.422470	62.387444	24.92	25.98	26.37	25.53	25.89	21.58	−1.0000
94.....	189.431992	62.351807	22.26	23.91	25.00	24.94	24.99	21.09	−1.0000
95.....	189.434677	62.396168	24.63	26.00	25.58	25.51	25.51	21.38	−1.0000
96.....	189.440475	62.307304	24.71	26.73	26.62	26.00	26.32	22.07	−1.0000
97.....	189.450241	62.065529	23.81	24.88	25.92	25.80	25.87	22.30	−1.0000
98.....	189.478958	62.156944	24.32	25.34	25.30	25.15	25.51	22.61	−1.0000
99.....	189.481674	62.404053	25.00	26.29	25.60	25.77	26.20	22.34	−1.0000
100.....	189.522583	62.161583	23.08	24.17	24.62	24.78	24.90	21.10	−1.0000
101.....	189.533249	62.261414	24.98	26.00	26.05	25.67	25.94	22.94	−1.0000
102.....	189.535751	62.391472	23.35	25.17	25.81	26.00	26.14	22.00	−1.0000
103.....	189.544647	62.049469	23.51	25.04	26.55	26.20	26.37	22.43	−1.0000
104.....	189.568802	62.259029	23.86	25.01	25.51	25.76	25.97	21.90	0.8353
105.....	189.582916	62.299004	24.07	25.38	25.48	25.64	25.82	21.91	0.8190
106.....	189.594589	62.139641	24.77	26.28	25.95	26.16	26.02	22.94	−1.0000
107.....	189.612747	62.258945	24.97	26.08	26.03	26.09	26.18	22.67	−1.0000
108.....	189.613754	62.330719	24.88	25.96	25.60	25.60	26.71	22.78	−1.0000
109.....	189.615387	62.313416	24.96	27.51	26.03	26.11	26.42	22.79	−1.0000
110.....	189.617569	62.367527	24.96	26.20	26.42	26.83	26.73	24.10	0.0000
111.....	334.186279	0.099167	24.48	99.00	26.99	27.29	26.61	26.74	0.0000
112.....	334.188812	0.211222	24.76	26.32	27.14	26.91	26.70	99.00	−1.0000
113.....	334.190338	0.092056	24.74	26.00	25.99	26.39	26.22	26.04	0.0000
114.....	334.192841	0.211722	23.20	24.24	24.85	25.40	25.66	25.83	−1.0000
115.....	334.197296	0.394167	24.59	25.62	26.79	25.28	25.20	24.92	−1.0000
116.....	334.206879	0.225333	24.75	25.78	26.32	27.23	24.60	99.00	−1.0000
117.....	334.206909	0.328528	24.54	25.72	99.00	99.00	99.00	99.00	0.0000
118.....	334.207733	0.425222	23.12	24.66	25.36	25.76	26.16	26.02	−1.0000
119.....	334.215912	0.082083	24.82	99.00	28.08	29.25	27.52	27.93	0.0000
120.....	334.220551	0.282694	23.91	25.58	26.22	26.24	26.70	27.35	−1.0000
121.....	334.233063	0.217056	22.13	23.28	23.78	24.12	24.47	24.18	−1.0000
122.....	334.233368	0.216306	23.22	25.20	25.77	26.03	25.98	25.71	0.8217
123.....	334.242035	0.108611	24.72	25.77	26.49	27.17	26.85	27.39	0.8196
124.....	334.241577	0.295056	24.48	25.72	25.38	25.90	28.67	27.35	0.0000
125.....	334.240631	0.321000	24.91	26.73	27.17	29.56	30.64	27.16	−1.0000
126.....	334.244965	0.383722	24.27	25.43	26.34	26.13	26.67	26.41	−1.0000
127.....	334.250854	0.204667	24.83	25.92	25.48	25.89	26.93	29.16	−1.0000
128.....	334.248566	0.185944	24.71	26.27	26.44	26.94	26.80	26.19	−1.0000
129.....	334.248962	0.336250	23.98	25.02	25.84	26.29	26.37	26.25	−1.0000

TABLE 3—*Continued*

Number (1)	R.A. (J2000.0) (2)	Decl. (J2000.0) (3)	$N(\text{AB})$ (4)	$z'(\text{AB})$ (5)	I (6)	R (7)	V (8)	B (9)	z_{spec} (10)
130.....	334.258972	0.220361	22.25	23.54	24.17	24.44	24.74	24.50	−1.0000
131.....	334.266937	0.389944	24.89	25.91	25.83	26.24	25.28	25.67	−1.0000
132.....	334.276459	0.065806	24.96	26.10	26.77	99.00	28.22	99.00	0.0000
133.....	334.273682	0.444417	23.53	24.62	25.08	26.06	26.07	26.87	−1.0000
134.....	334.282776	0.153917	22.19	23.39	23.90	24.29	24.61	24.31	−1.0000
135.....	334.286285	0.083139	24.62	25.65	25.84	26.51	26.64	26.14	−1.0000
136.....	334.288544	0.401167	23.66	25.08	25.57	26.08	27.04	25.91	−1.0000
137.....	334.289459	0.459583	23.37	24.99	25.73	26.19	26.34	26.35	−1.0000
138.....	334.295624	0.378667	24.99	26.10	25.76	26.21	26.71	25.97	−1.0000
139.....	334.299133	0.461778	22.60	23.91	24.51	24.92	25.23	25.07	−1.0000
140.....	334.306274	0.207806	24.95	26.21	25.36	25.84	26.39	27.89	0.0000
141.....	334.314606	0.232694	24.07	25.17	25.37	25.82	26.04	25.40	−1.0000
142.....	334.312714	0.430556	24.85	26.21	26.17	26.95	26.44	26.21	−1.0000
143.....	334.318298	0.278333	22.81	24.42	25.42	25.59	27.11	25.88	0.8186
144.....	334.321899	0.156528	24.83	26.10	26.49	26.53	26.68	26.36	−1.0000
145.....	334.321381	0.169139	24.13	25.34	26.11	26.70	26.68	26.30	−1.0000
146.....	334.328796	0.130306	23.73	25.11	26.04	26.47	26.40	26.12	0.8217
147.....	334.335785	0.119333	22.80	23.87	24.36	24.85	25.22	25.13	0.8216
148.....	334.337494	0.075500	23.71	24.97	25.36	26.13	26.35	26.35	0.8259
149.....	334.343201	0.262417	24.56	26.68	26.18	26.94	26.85	26.70	0.8342
150.....	334.342255	0.429583	24.85	26.02	26.07	26.24	26.25	26.03	−1.0000
151.....	334.340485	0.246972	21.56	23.11	24.27	24.41	24.62	24.41	−1.0000
152.....	334.347046	0.361917	24.97	26.28	26.93	27.30	99.00	28.50	−1.0000
153.....	334.347046	0.361917	22.38	23.43	23.96	24.37	24.77	24.64	−1.0000
154.....	334.347870	0.272389	21.91	23.41	24.32	24.49	24.81	24.59	−1.0000
155.....	334.357880	0.050472	23.99	25.00	25.22	25.83	99.00	99.00	−1.0000
156.....	334.357422	0.188667	23.93	25.00	25.82	26.53	26.92	27.27	0.0000
157.....	334.358795	0.221861	23.55	25.25	25.79	26.39	27.25	26.10	−1.0000
158.....	334.362213	0.438750	24.37	25.57	26.27	26.87	26.76	27.81	−1.0000
159.....	334.363953	0.197278	22.73	23.84	24.05	24.01	24.40	24.47	0.3954
160.....	334.365082	0.146944	23.49	24.87	25.65	25.93	26.96	26.16	−1.0000
161.....	334.374329	0.077667	24.11	25.24	25.85	26.02	26.24	26.01	−1.0000
162.....	334.377350	0.187500	22.63	23.74	24.24	24.70	25.10	24.76	−1.0000
163.....	334.383057	0.262278	22.58	23.69	24.27	24.74	24.98	24.70	0.8338
164.....	334.384857	0.153694	23.24	24.87	26.01	26.37	27.46	26.04	−1.0000
165.....	334.385132	0.267861	24.97	26.02	25.82	26.00	26.41	26.43	−1.0000
166.....	334.392883	0.300056	24.21	25.59	26.40	27.15	27.85	27.17	−1.0000
167.....	334.391113	0.440472	24.98	26.12	25.38	25.83	26.25	26.75	−1.0000
168.....	334.393585	0.133917	23.88	25.01	25.04	25.79	26.02	25.71	−1.0000
169.....	334.400269	0.341667	23.17	24.25	24.44	24.81	25.08	24.93	−1.0000
170.....	334.400940	0.208083	24.65	25.75	25.83	26.23	26.99	26.74	1.4471
171.....	334.405212	0.343194	24.20	25.39	25.38	25.69	26.23	25.74	−1.0000
172.....	334.407562	0.638278	23.75	24.97	25.37	25.79	26.49	26.68	0.8262
173.....	334.411072	0.445222	24.56	25.74	25.69	25.75	25.83	25.33	−1.0000
174.....	334.409973	0.152639	24.82	27.21	99.00	99.00	99.00	29.19	6.4825
175.....	334.417572	0.137333	24.80	26.41	28.55	27.75	27.78	99.00	0.0000
176.....	334.417572	0.132167	24.34	25.60	25.54	25.93	26.14	25.42	−1.0000
177.....	334.417664	0.176389	24.92	26.14	26.56	26.63	27.18	26.33	−1.0000
178.....	334.416382	0.295222	24.28	25.70	26.19	26.76	26.02	26.22	−1.0000
179.....	334.417511	0.208222	24.63	25.64	25.66	25.95	25.82	25.86	−1.0000
180.....	334.421295	0.526306	24.37	26.96	102.35	102.18	101.99	101.63	6.5047
181.....	334.422882	0.406028	23.77	24.93	24.70	24.81	25.43	25.72	−1.0000
182.....	334.429260	0.302361	24.16	25.95	99.00	99.00	99.00	99.00	6.4700
183.....	334.430176	0.204556	24.19	25.32	25.67	26.11	26.21	26.18	−1.0000
184.....	334.432739	0.308333	23.56	24.73	24.96	25.47	25.38	25.37	−1.0000
185.....	334.436249	0.468556	23.56	24.65	24.84	25.44	25.91	25.50	−1.0000
186.....	334.437714	0.251944	24.97	26.00	26.40	26.47	27.09	26.95	0.0000
187.....	334.437531	0.464917	22.45	23.54	23.78	24.25	24.62	24.37	−1.0000
188.....	334.441467	0.460444	23.18	24.71	25.30	25.61	25.46	25.65	0.0000
189.....	334.442108	0.214167	23.28	24.47	25.56	25.65	26.35	26.04	0.8152
190.....	334.443359	0.303500	23.11	24.74	25.57	25.72	26.19	25.47	0.8182
191.....	334.445374	0.250750	23.23	24.78	25.41	25.47	25.71	25.70	0.8221
192.....	334.445465	0.355389	24.01	25.72	25.59	26.14	26.71	26.03	−1.0000
193.....	334.453400	0.180944	24.76	26.39	26.14	26.48	26.28	27.78	−1.0000
194.....	334.456696	0.807056	24.85	27.69	102.35	102.18	101.99	101.63	0.0000

TABLE 3—*Continued*

Number (1)	R.A. (J2000.0) (2)	Decl. (J2000.0) (3)	<i>N</i> (AB) (4)	<i>z'</i> (AB) (5)	<i>I</i> (6)	<i>R</i> (7)	<i>V</i> (8)	<i>B</i> (9)	<i>z</i> _{spec} (10)
195.....	334.454742	0.208917	24.30	25.59	25.61	25.99	25.87	25.53	−1.0000
196.....	334.458710	0.355278	24.04	25.20	25.23	25.33	26.09	25.21	−1.0000
197.....	334.460144	0.057361	24.10	25.52	25.96	26.13	26.96	27.80	0.8207
198.....	334.465179	0.435194	24.98	26.74	25.97	26.52	26.81	26.85	−1.0000
199.....	334.465454	0.133528	24.96	26.17	26.06	26.56	27.41	26.90	−1.0000
200.....	334.466522	0.312611	20.84	22.69	23.71	23.75	23.93	23.54	−1.0000
201.....	334.468140	0.601722	24.55	25.70	26.16	25.92	26.28	26.26	−1.0000
202.....	334.471039	0.149167	23.60	24.66	25.06	25.42	25.90	25.17	−1.0000
203.....	334.474854	0.291944	24.30	25.32	25.31	25.87	26.66	26.14	−1.0000
204.....	334.474457	0.469000	24.77	25.94	24.89	25.06	25.76	25.64	−1.0000
205.....	334.476166	0.686500	22.35	23.68	24.32	23.31	24.06	24.51	0.3981
206.....	334.477966	0.130000	25.00	26.53	25.89	26.31	26.88	26.40	−1.0000
207.....	334.477264	0.060083	23.66	24.77	25.43	25.95	26.78	26.02	0.8225
208.....	334.477753	0.470667	24.62	25.63	25.48	25.67	25.70	26.03	−1.0000
209.....	334.480377	0.502056	24.30	25.62	26.85	26.58	26.92	27.52	0.8233
210.....	334.483337	0.593694	24.99	26.72	26.97	27.14	28.08	28.38	0.8270
211.....	334.482147	0.255861	24.86	26.49	27.81	29.77	99.00	29.35	0.0000
212.....	334.483337	0.357194	24.78	25.88	25.36	26.01	26.36	26.61	−1.0000
213.....	334.483551	0.238139	24.74	26.23	25.91	25.91	26.76	27.09	−1.0000
214.....	334.486786	0.155917	24.97	26.03	26.31	26.63	26.46	26.65	−1.0000
215.....	334.485626	0.289028	24.84	26.26	25.45	25.70	26.12	25.81	−1.0000
216.....	334.488708	0.305222	24.84	27.27	28.97	27.36	99.00	27.14	0.0000
217.....	334.490845	0.613556	24.54	25.56	25.78	26.02	26.29	26.30	0.0000
218.....	334.506470	0.236556	23.95	25.48	26.62	26.50	99.00	27.27	0.0000
219.....	334.505402	0.282750	21.86	23.05	23.73	23.98	24.33	24.06	0.8206
220.....	334.506073	0.312167	24.96	26.15	25.70	26.09	27.98	26.88	−1.0000
221.....	334.506470	0.326278	24.89	26.01	25.21	25.69	99.00	31.08	−1.0000
222.....	334.505066	0.473056	23.85	24.88	25.40	25.94	26.41	26.41	0.8233
223.....	334.507080	0.274083	22.86	24.14	24.68	25.34	99.00	25.87	0.8209
224.....	334.506805	0.327611	24.59	25.67	25.37	26.01	99.00	26.11	−1.0000
225.....	334.507874	0.812278	24.62	28.39	27.99	27.12	26.65	27.45	6.5180
226.....	334.510406	0.374194	24.84	26.00	25.82	25.87	25.87	26.05	−1.0000
227.....	334.513153	0.468778	24.72	26.03	25.45	25.81	26.12	26.24	−1.0000
228.....	334.515198	0.462917	24.81	25.84	25.05	25.45	25.64	25.75	−1.0000
229.....	334.513153	0.468778	24.75	26.09	25.50	26.06	26.13	27.32	−1.0000
230.....	334.516235	0.425500	24.88	26.00	25.75	25.99	25.72	26.06	−1.0000
231.....	334.516235	0.379750	24.99	26.03	25.83	25.83	25.79	26.39	−1.0000
232.....	334.523346	0.325583	23.33	24.44	24.44	24.84	25.11	24.70	0.8420
233.....	334.520691	0.446389	23.42	24.81	24.87	25.28	25.78	25.72	−1.0000
234.....	334.523499	0.428639	24.96	26.23	25.70	26.55	26.05	26.20	−1.0000
235.....	334.526031	0.361667	24.74	26.05	25.89	26.99	27.19	26.65	−1.0000
236.....	334.525177	0.359083	24.66	25.90	26.02	27.44	−99.00	27.10	0.0000
237.....	334.537323	0.349167	22.68	23.76	23.86	24.10	24.19	24.01	1.4864
238.....	334.537323	0.490111	22.99	24.00	24.44	24.61	25.02	25.06	0.8180
239.....	334.542847	0.440722	21.10	22.13	22.29	22.77	23.12	23.04	0.8273
240.....	334.541168	0.398083	23.22	24.85	25.23	25.66	26.12	25.60	0.8293
241.....	334.541168	0.398083	24.77	26.01	25.92	26.73	26.60	27.60	−1.0000
242.....	334.543762	0.062000	22.70	24.06	24.64	25.01	25.28	25.01	−1.0000
243.....	334.543762	0.311417	24.88	26.30	25.29	25.68	26.28	26.97	−1.0000
244.....	334.545105	0.067000	24.79	26.95	99.00	99.00	99.00	99.00	0.0000
245.....	334.548492	0.052167	24.70	25.78	25.35	25.39	25.46	99.00	−1.0000
246.....	334.548462	0.335722	24.80	26.69	26.01	26.38	26.61	25.89	−1.0000
247.....	334.548187	0.398528	24.67	25.83	25.83	26.97	99.00	99.00	−1.0000
248.....	334.575500	0.534444	24.54	25.61	25.86	25.92	26.38	26.51	−1.0000
249.....	334.580109	0.606139	22.97	24.13	24.87	24.93	25.17	25.29	0.8274
250.....	334.583466	0.681194	24.29	25.39	26.21	26.09	26.21	26.21	0.8295
251.....	334.591522	0.653972	24.95	26.26	26.84	26.75	27.16	27.42	−1.0000
252.....	334.605072	0.570444	23.69	24.70	25.30	25.24	25.57	25.60	0.8294
253.....	334.614990	0.423056	24.92	27.47	26.56	27.11	31.25	27.91	−1.0000
254.....	334.615173	0.791028	24.89	28.16	102.35	102.18	101.99	101.63	6.5050
255.....	334.625763	0.424972	24.60	25.67	25.99	25.77	26.04	26.08	−1.0000
256.....	334.623962	0.524361	23.15	24.24	24.61	24.05	24.64	24.98	−1.0000
257.....	334.627350	0.752278	24.39	25.75	26.14	26.19	27.05	26.94	−1.0000
258.....	334.638947	0.521500	24.05	25.18	25.72	25.67	26.00	26.05	−1.0000
259.....	334.647644	0.507778	23.63	25.13	25.34	25.23	25.75	25.92	−1.0000

TABLE 3—*Continued*

Number (1)	R.A. (J2000.0) (2)	Decl. (J2000.0) (3)	$N(\text{AB})$ (4)	$z'(\text{AB})$ (5)	I (6)	R (7)	V (8)	B (9)	z_{spec} (10)
260.....	334.654755	0.814722	24.58	25.70	25.76	25.72	26.20	26.90	0.8289
261.....	334.666840	0.422056	24.21	25.25	25.13	25.14	25.26	25.07	1.4627
262.....	334.670563	0.618389	24.42	25.52	26.00	25.95	26.16	26.41	0.8252
263.....	334.668457	0.684972	24.94	26.78	26.48	26.62	27.32	26.73	−1.0000
264.....	334.670563	0.646028	24.89	25.93	26.43	26.38	26.45	27.22	0.0000
265.....	334.687927	0.550639	24.93	26.20	26.60	26.50	26.73	26.98	0.0000
266.....	334.721222	0.693750	22.68	24.08	24.76	23.56	24.34	24.68	0.3987
267.....	334.749329	0.561972	23.59	24.62	25.20	25.29	25.40	25.56	0.8269
268.....	334.750763	0.582028	23.94	25.60	26.20	26.14	26.65	26.54	0.8276
269.....	334.751465	0.471639	24.54	25.55	25.74	26.23	27.36	26.58	0.0000
270.....	334.776215	0.789361	23.24	24.48	25.38	25.29	25.50	25.52	0.8176
271.....	334.788086	0.441750	23.95	25.18	25.44	25.60	25.96	25.80	0.8320
272.....	334.792847	0.570306	24.93	25.94	25.99	25.98	26.33	26.19	−1.0000
273.....	334.794342	0.735417	23.72	24.80	25.15	25.33	25.61	25.78	0.8270
274.....	334.796967	0.674806	24.63	25.72	26.44	26.16	26.43	26.75	−1.0000
275.....	334.797302	0.724806	24.89	26.30	26.44	25.97	26.97	27.68	−1.0000

NOTES.—Magnitudes are measured in 3" diameter apertures. An entry of "−99" indicates that no excess flux was measured, while "99" means that there was a negative flux in the aperture. A value of −1.0000 in the redshift column means that no spectroscopic data were obtained for the object, 0.0000 means that spectra were obtained, but the object was not identified, while −2.0000 denotes a star.

reason why we force-fitted the position and line widths of the Gaussian and allowed only the normalization to vary when fitting the weak lines. We have adopted a very conservative 10% systematic error in the [O III] $\lambda 4959$ line where the full Gaussian fitting procedure was used.

The brighter objects may be absolutely calibrated using the continuum magnitudes obtained from our Subaru data. We integrated the spectrum convolved with each SuprimeCam filter response and set this equal to the broadband flux to normalize the spectrum in each of the filters. We then used the Gaussian fits to obtain the spectral line fluxes for lines lying within that broad band. This procedure only works for sources with well-determined continuum magnitudes ($C < 24.5$) where the sky subtraction can be well determined in the spectra. For these objects the spectrally determined fluxes are shown versus the primary fluxes in Figure 10, where we plot the ratio of the spectral to the primary flux versus the primary line flux. The values agree extremely well although the measured spectral line fluxes are on average about 80%–90% of the primary flux values. This may reflect a selection bias in the choice of the objects, or the narrowband filters could be slightly narrower than the nominal profiles.

4.3. Balmer Ratios

We then measured the Balmer ratios for the sample of objects selected in $H\alpha$ and where the continuum magnitudes were bright enough to absolutely flux-calibrate the spectra. The ratio of $f(H\beta)/f(H\alpha)$ is shown in Figure 11. The values average closely to the case B ratio, which is shown as the solid line, and at brighter fluxes the individual values also closely match this value, suggesting that the galaxies have very little reddening. However, at fainter fluxes the scatter about the average value is considerably higher than the statistical errors. At the faintest fluxes it appears that the systematic uncertainty can be as high as a multiplicative factor of 2.

4.4. Final Flux Calibration for Metallicity Analysis

For the metallicity analysis we adopted the procedure of normalizing the longer wavelength lines ([O III] $\lambda\lambda 4959, 5007$, [O III] $\lambda 4363$) to their nearest Balmer line to determine the un-

reddened fluxes. For example, in the case of the $H\alpha$ emission-selected galaxies, we can measure $H\alpha$ absolute fluxes by the primary flux method described in § 4.1. We can then derive $H\beta$ and $H\gamma$ fluxes from $H\alpha$ fluxes by assuming case B recombination [e.g., $f(H\alpha) = 2.85f(H\beta)$, $f(H\gamma) = 0.469f(H\beta)$ at $T = 10^4$ K and $N_e \sim 10^2$ – 10^4 cm $^{-3}$; Osterbrock 1989]. As $H\beta$ and [O III] $\lambda\lambda 4959, 5007$ have very similar DEIMOS responses, the relative fluxes should remain the same with or without the flux calibration, and this can be expressed by a simple equation:

$$\frac{f_0(H\beta)}{f_0([\text{O III}] \lambda\lambda 4959, 5007)} = \frac{f(H\beta)}{f([\text{O III}] \lambda\lambda 4959, 5007)},$$

where $f_0(H\beta)$ and $f_0([\text{O III}] \lambda\lambda 4959, 5007)$ are the flux counts in the uncalibrated, reddened DEIMOS spectra, while $f(H\beta)$ and $f([\text{O III}] \lambda\lambda 4959, 5007)$ are absolute, unreddened fluxes. Since we know $f(H\beta)$ from $f(H\alpha)$ with the case B assumption and $f_0(H\beta)/f_0([\text{O III}] \lambda\lambda 4959, 5007)$ from the DEIMOS spectra, we can derive $f([\text{O III}] \lambda\lambda 4959, 5007)$ using this simple formula. Similarly, we can absolutely calibrate [O III] $\lambda 4363$ lines by using its neighboring Balmer line, $H\gamma$:

$$\frac{f_0(H\gamma)}{f_0([\text{O III}] \lambda 4363)} = \frac{f(H\gamma)}{f([\text{O III}] \lambda 4363)},$$

where $f_0(H\gamma)$ and $f_0([\text{O III}] \lambda 4363)$ are again the counts in flux-uncalibrated, reddened DEIMOS spectra and $f(H\gamma)$ and $f([\text{O III}] \lambda 4363)$ are absolute fluxes.

In the case of the [O III]–selected emitters, we first derive [O III] $\lambda\lambda 4959, 5007$ absolute fluxes using the primary flux method (§ 4.1) and then use the above formula to get absolute fluxes of $H\beta$, then $H\gamma$ (by the case B ratio), and finally [O III] $\lambda 4363$.

This flux calibration technique using the neighboring Balmer line should work well for the [O III] $\lambda\lambda 4959, 5007, 4363$ lines and the [N II] lines, which all lie close to Balmer lines but may be slightly more approximate for the [S II] lines. The higher order Balmer lines are too uncertain to apply this procedure due to inadequate signal-to-noise ratio (S/N) of the lines, and we have used the continuum flux-calibrated values with no reddening

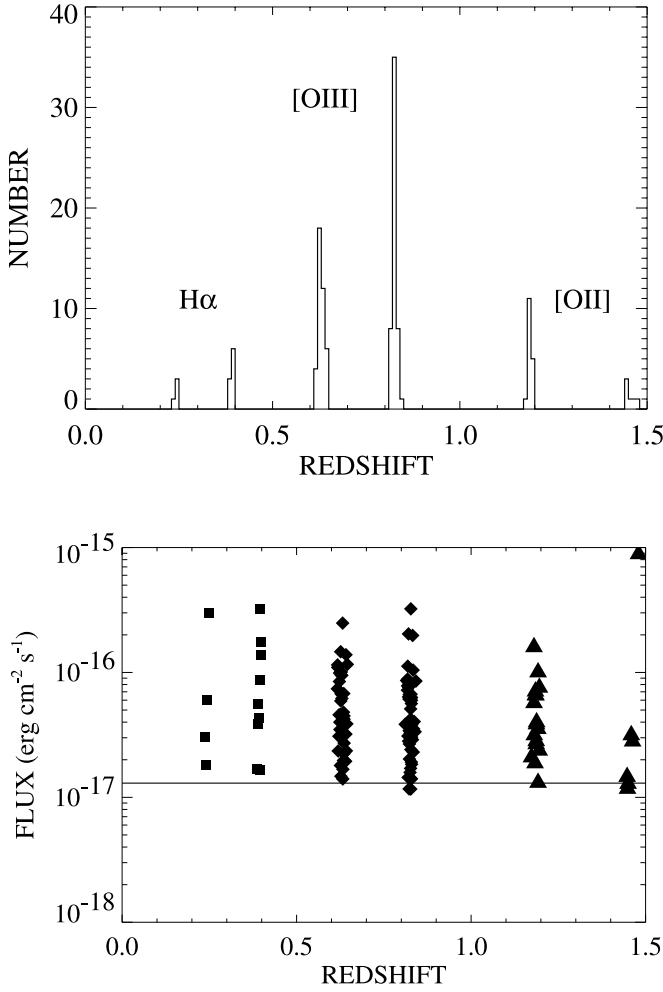


FIG. 7.—*Top*: Distribution of redshifts for the spectroscopically identified sources. [O III] $\lambda 5007$ emitters are the most common. Since the focus of this paper is on intermediate-redshift ($z \lesssim 1$) strong emission line galaxies, we did not plot the high-redshift Ly α galaxies ($z \gg 5$) in our sample. High- z Ly α emitters are discussed in Hu et al. (2004) and E. M. Hu (2007, in preparation). *Bottom*: Flux vs. redshift for the spectroscopically identified sample. Squares are H α , diamonds are [O III] $\lambda 5007$, and triangles are [O II] $\lambda 3727$. The solid line shows the flux limit corresponding to the narrowband magnitude limit of $N(\text{AB}) = 25$ for an emitter with very large equivalent width. Some objects with lower equivalent widths fall below this limit.

for the [O II] $\lambda 3727$ and [Ne III] lines. These values will have correspondingly higher flux uncertainties. Fortunately, the [O II] $\lambda 3727$ line is very weak in most of the objects and the uncertainty has little effect on the metallicity determinations. However, ionization analyses based on the [Ne III] line should be undertaken with caution.

5. STAR FORMATION HISTORY

5.1. H α and [O III] $\lambda 5007$ Luminosity Functions

Because of the high observed-frame equivalent widths, the primary fluxes are insensitive to the continuum determination. However, they do depend on the filter response at the emission-line wavelength so we first restrict ourselves to redshifts where the nominal filter response is greater than 70% of the peak value. This also has the advantage of providing a uniform selection, and we assume that the window function is flat over the defined redshift range. Now the volume is simply defined by the selected redshift range for all objects above the minimum luminosity, which we take as corresponding to a flux of 1.5×10^{-17} ergs cm $^{-2}$ s $^{-1}$

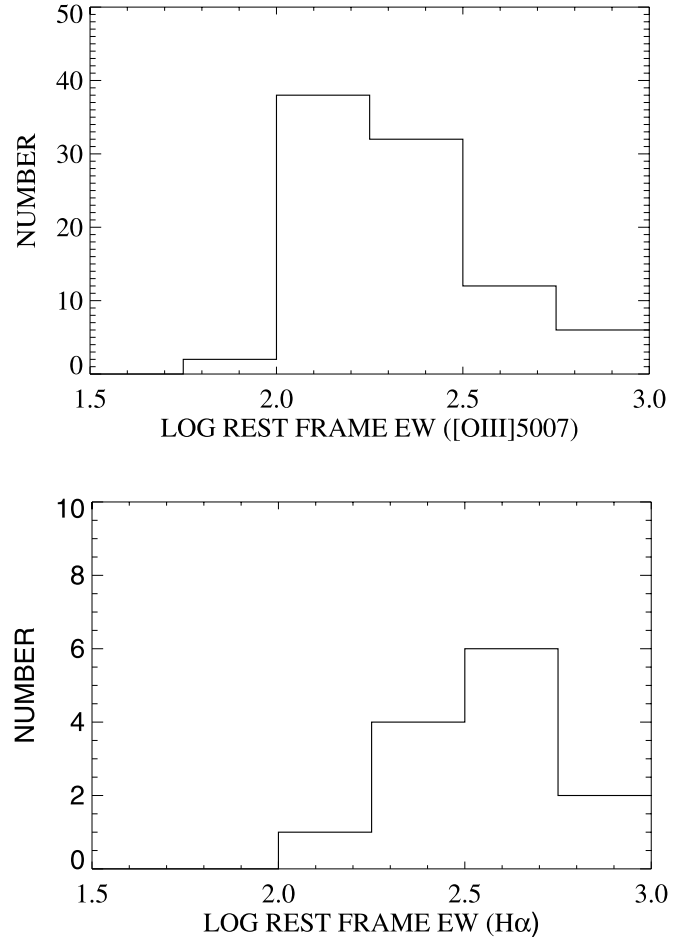


FIG. 8.—*Top*: Distribution of the rest-frame equivalent widths determined from the narrowband magnitudes for the spectroscopically identified [O III] $\lambda 5007$ sources. *Bottom*: Distribution of the rest-frame equivalent widths for the H α -selected sample.

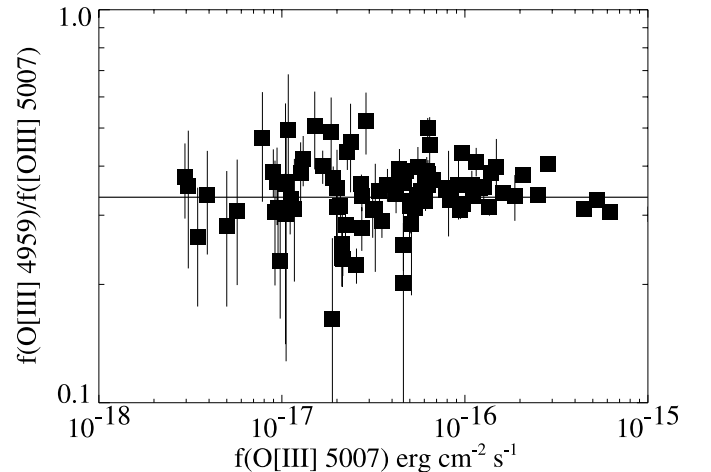


FIG. 9.—Ratio of the [O III] $\lambda 4959$ line to [O III] $\lambda 5007$. The errors are $\pm 1 \sigma$. The median ratio is 0.338, and the scatter around this value is consistent with that expected from the statistical errors. However, a small systematic upward trend in the ratio can be seen as we move to the weaker fluxes. This is a consequence of the full Gaussian fits slightly overestimating the fluxes of weak lines. We have assigned a 10% systematic error to the [O III] $\lambda 4959$ and [O III] $\lambda 5007$ fluxes to allow for this effect.

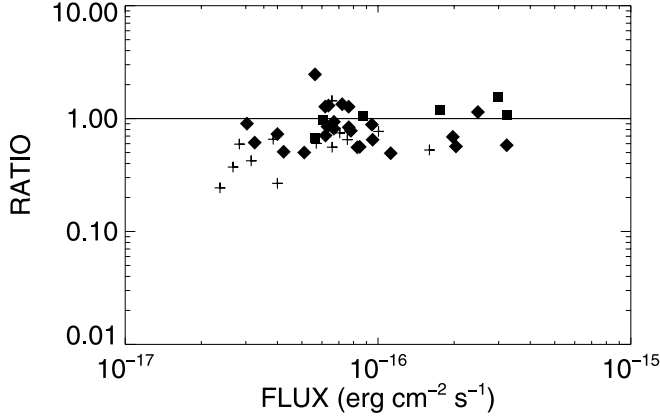


FIG. 10.—Ratio of fluxes computed from the spectra and the broadband magnitudes vs. those from the narrowband magnitudes. $H\alpha$ lines are shown as filled squares, $[O\text{ III}] \lambda 5007$ lines as filled diamonds, and $[O\text{ II}] \lambda 3727$ lines as plus signs.

(Fig. 7). The luminosity function is now obtained by dividing the number of objects in each luminosity bin by the volume. The incompleteness-corrected luminosity function is obtained from the sum of the weights in each luminosity bin divided by the volume. The 1σ errors shown are calculated from the Poissonian errors based on the number of objects in the bin. The calculated $H\alpha$ luminosity function is shown for the two redshift ranges corresponding to the NB816 and NB912 selections in Figure 12 and the corresponding $[O\text{ III}] \lambda 5007$ luminosity functions in Figure 13.

5.2. Star Formation Rates

The individual objects have $H\alpha$ luminosities stretching up to about 3×10^{41} ergs s^{-1} where, at the higher redshifts, we use the $H\beta$ luminosity to infer the $H\alpha$ value assuming that there is no reddening. For a steady formation this would require an SFR of a few solar masses per year if we adopt the Kennicutt (1998) conversion rate for his Salpeter mass function.

Since the objects are more probably caused by starbursts, the true SFR will depend on the evolutionary history. However, the $H\alpha$ luminosity density should give a reasonable estimate of the universal star formation density of the objects provided only that most of the ionizing photons are absorbed in the galaxies. We

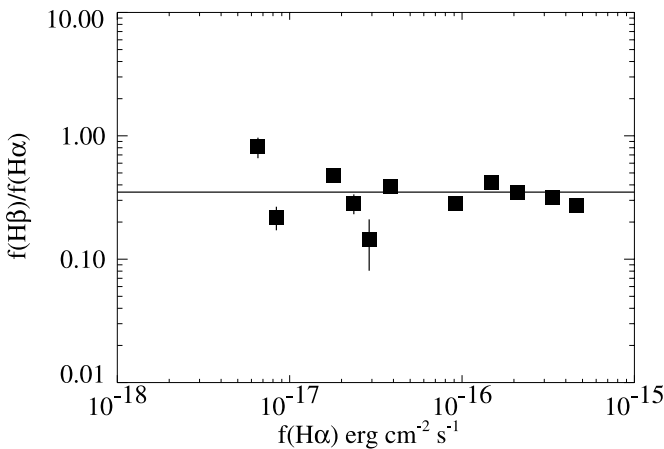


FIG. 11.—Ratio of the $H\beta/H\alpha$ fluxes vs. $H\alpha$ flux. The values average to the unreddened Balmer decrement shown by the solid line, but at the lower fluxes the scatter is larger than expected from the statistical errors, reflecting the calibration uncertainties for the fainter sources. The figure shows the 10 objects detected in the $H\alpha$ line with continuum magnitudes above 24.5 in the bandpasses corresponding to the lines.

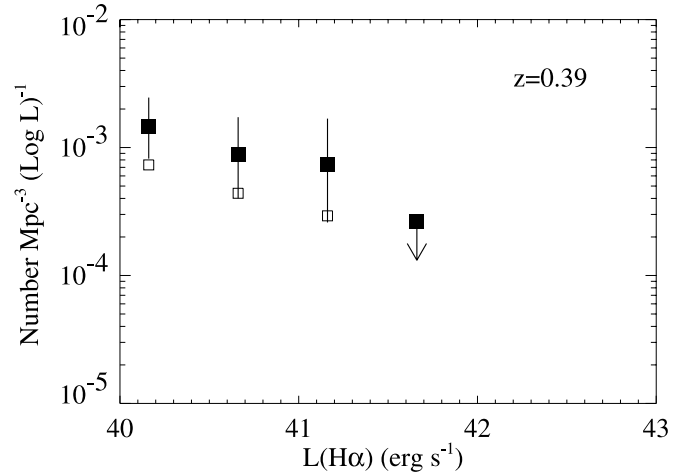
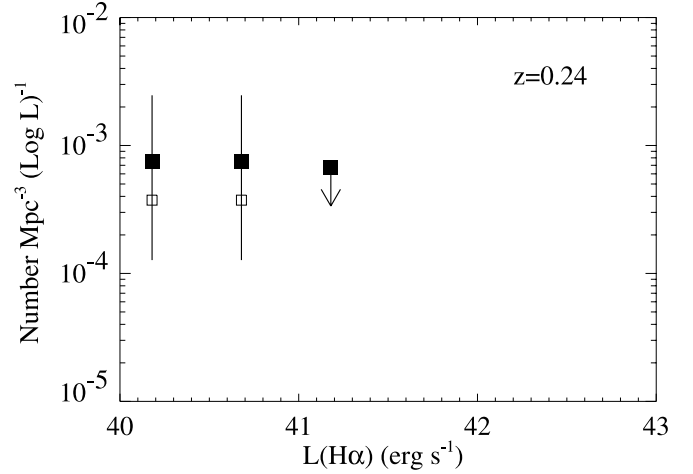


FIG. 12.—Luminosity function of $H\alpha$ at $z = 0.24$ (top) and $z = 0.39$ (bottom). In each case the open squares show the luminosity functions determined from the spectroscopic sample alone, while the filled squares show the function corrected for the incompleteness in the spectroscopic identification. The errors are $\pm 1\sigma$, and at the highest luminosity we show the 1σ upper limit.

first formed the total $H\alpha$ or $H\beta$ luminosity density of the galaxies by summing over the incompleteness-weighted luminosities in each redshift interval. We only included detected objects and did not attempt to extrapolate to lower luminosities, but the results are not particularly sensitive to this because the luminosity functions are relatively flat at the lower luminosities (Figs. 12 and 13). We then converted these to SFRs with the Kennicutt (1998) conversion.

The results are shown in Figure 14. We first plot the rate for the total samples at each redshift, shown by the open squares. We have shown SFRs for UV continuum samples for comparison, and the present sample of strong emitters gives SFRs that are about 10% of the UV values over the redshift interval. For comparison, we also show the SFRs from $H\alpha$ -selected samples reported in the literature and summarized in Ly et al. (2007). In order to better understand the evolution, we have also restricted our own sample to objects with rest-frame equivalent widths of $H\alpha$ in excess of 200 \AA at low redshifts and $H\beta$ equivalent widths in excess of 70 \AA at higher redshifts. The SFRs for this sample are shown with the filled squares. This provides a more uniform selection with redshift and gives a slower increase than the total inferred SFR. For this sample the SFR is evolving roughly as $(1+z)^3$, broadly similar to other UV and optically determined

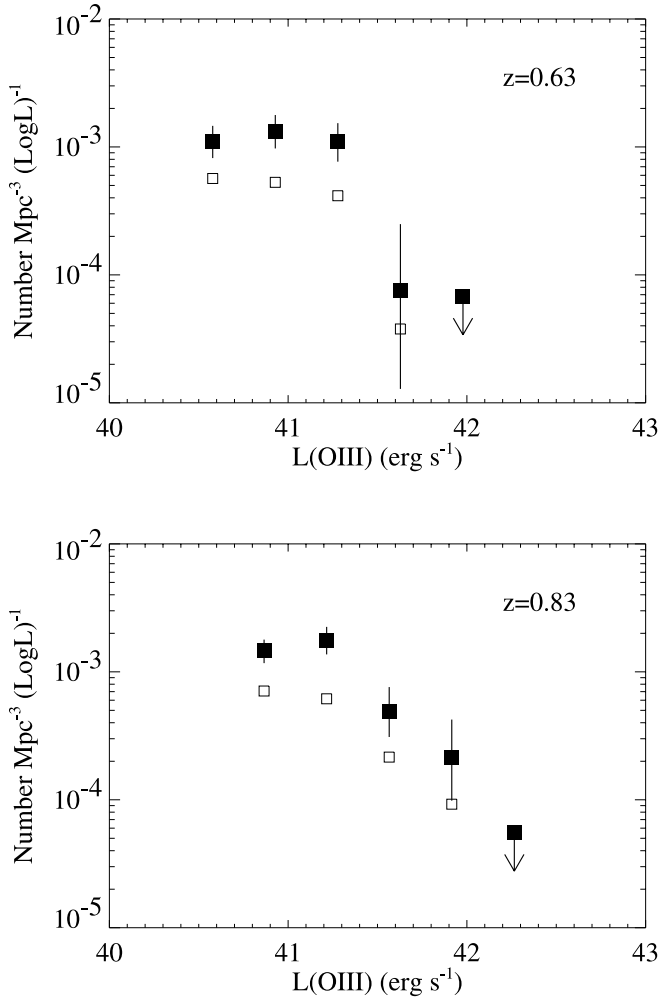


FIG. 13.—Luminosity function of $[\text{O III}] \lambda 5007$ emitters at $z = 0.63$ (top) and $z = 0.83$ (bottom). In each case the open squares show the luminosity functions determined from the spectroscopic sample alone, while the filled squares show the function corrected for the incompleteness in the spectroscopic identification. The errors are $\pm 1 \sigma$, and at the highest luminosity we show the 1σ upper limit.

formation rates in this redshift interval. These more restricted objects comprise about 5% relative to the UV SFRs at higher redshifts.

6. GALAXY METALLICITIES

6.1. $[\text{O III}]$ Emitters

The spectra are of variable quality, and in order to measure the metallicities, we need very high S/N observations. It is also important that Balmer lines are well detected since our flux calibrations are done using the neighboring Balmer lines (§ 4.4). We therefore restricted ourselves to $[\text{O III}]$ emitters whose $\text{H}\beta$ fluxes are detected above 15σ . Among 92 $[\text{O III}]$ emitters in our total spectroscopic sample, 8 such $[\text{O III}]$ emitters were chosen in the NB912 sample, and 10 in the NB816 sample. These emitters have $\text{H}\gamma$ detected above 4σ . Tables 4 and 5 give the oxygen line fluxes normalized by their $\text{H}\beta$ fluxes for the NB816- and NB912-selected emitters, respectively. The 1σ upper limits are listed when the measured flux is below 1σ .

The most direct method to estimate the gas-phase oxygen abundance is to use the electron temperature of the H II region. Higher gas metallicity increases nebular cooling, leading to lower electron temperatures. Therefore, electron temperature is a good indicator of the gas metallicity. The electron temperature can be derived from the ratio of the $[\text{O III}] \lambda 4363$ auroral line to $[\text{O III}]$

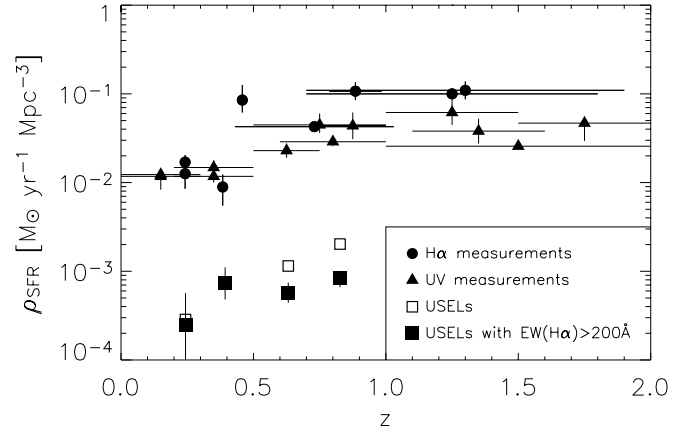


FIG. 14.—Star formation history inferred from the $\text{H}\alpha$ or $\text{H}\beta$ luminosity density as a function of redshift. The data from our sample are shown with open and filled boxes. The open squares show the total rate from the entire sample, while the filled squares show the values for objects with $\text{H}\alpha$ rest-frame equivalent widths in excess of 200 \AA or $\text{H}\beta$ rest-frame equivalent widths in excess of 70 \AA . The diamonds show the UV SFRs (uncorrected for extinction) from the ground-based work of Wilson et al. (2002), and the triangles the GALEX results of Wyder et al. (2005) and Schiminovich et al. (2005). $\text{H}\alpha$ measurements from the literature as summarized in Ly et al. (2007) are shown with filled circles. In all cases the errors are $\pm 1 \sigma$. [See the electronic edition of the Journal for a color version of this figure.]

$\lambda\lambda 5007, 4959$. This procedure is often referred to as the “direct” method or T_e method (e.g., Seaton 1975; Pagel et al. 1992; Pilyugin & Thuan 2005; Izotov et al. 2006b). One well-known problem with the direct method, however, is that $[\text{O III}] \lambda 4363$ is generally very weak even in the low-metallicity galaxies. For higher metallicity systems, the far-IR lines become the dominant coolant and therefore the optical auroral line is essentially not detectable. However, the majority of our sample exhibits $[\text{O III}] \lambda 4363$, already suggesting that these are metal-deficient systems. To derive $T_e[\text{O III}]$ and the oxygen abundances, we used the Pagel et al. (1992) calibrations with the $T_e[\text{O II}]$ – $T_e[\text{O III}]$ relations derived by Garnett (1992). The results are shown in Table 4 (for NB816-selected $[\text{O III}]$ emitters) and Table 5 (for NB912-selected $[\text{O III}]$ emitters). The Izotov et al. (2006b) formula, which was developed with the latest atomic data and photoionization models, gives consistent abundances within 0.1 dex. The $[\text{S II}] \lambda\lambda 6717, 6731$ lines that are usually used for the determination of the electron number density are beyond the Keck DEIMOS wavelength coverage for our $[\text{O III}]$ emitters. Therefore, we assumed $n_e = 100 \text{ cm}^{-3}$. However, the choice of electron density has little effect as electron temperature is insensitive to the electron density; indeed, we get the same results even when we use $n_e = 1000 \text{ cm}^{-3}$.

The 1σ upper and lower limits on $T_e[\text{O III}]$ and the oxygen abundances are also shown in the tables. Because the $[\text{O III}] \lambda 4363$ fluxes are weak, the range of our metallicity measurements is quite wide. However, of 18 $[\text{O III}]$ emitters, even the upper metallicity limits on 6 emitters satisfy the definition of XMPGs [$12 + \log(\text{O}/\text{H}) < 7.65$; Kunth & Östlin 2000]. All our emitters, except the ones that only have lower limits on metallicities such as NB816-selected USEL 31 in Table 4, have very low metallicities: even the upper metallicity limits are about 0.02 – $0.2 Z_\odot$. A few emitters may even have metallicities that are comparable to the currently known most metal-poor galaxies [I Zw 18 and SBS 0335–052W; $12 + \log(\text{O}/\text{H}) \sim 7.1$ – 7.2]. However, our current metallicity errors are too large to measure the baseline metallicity accurately, and higher S/N spectra will be necessary for this purpose.

TABLE 4
LINE FLUXES AND OXYGEN ABUNDANCE FOR NB816-SELECTED USELS

Object	$f([\text{O III}] \lambda 5007)$	$f([\text{O III}] \lambda 4959)$	$f([\text{O III}] \lambda 4363)$	$f([\text{O II}] \lambda 3727)$	$T_e[\text{O III}]$ (10^4 K)	$12 + \log(\text{O/H})$	$12 + \log(\text{O/H})^a$
[O III] Emitters							
31.....	513.6 ± 24.0	222.3 ± 11.4	<6.60	54.4 ± 4.62	<1.19	>8.09	7.74 ± 0.02
40.....	577.9 ± 21.6	191.3 ± 8.05	9.40 ± 3.40	140.9 ± 6.22	$1.14 < 1.34 < 1.53$	$7.86 < 8.03 < 8.25$	7.84 ± 0.02
51.....	401.5 ± 12.6	146.9 ± 5.52	9.40 ± 4.50	...	$1.19 < 1.55 < 1.90$	$7.51 < 7.62 < 7.94$...
76.....	464.4 ± 10.5	191.3 ± 4.86	<2.90	344.5 ± 8.07	<0.95	>8.55	7.89 ± 0.01
118.....	492.6 ± 29.7	193.9 ± 12.9	34.4 ± 12.8	11.3 ± 2.61	$2.16 < 3.08 < 4.32$	$6.93 < 7.16 < 7.44$	7.67 ± 0.03
195.....	335.0 ± 21.4	129.5 ± 10.2	24.0 ± 10.9	97.1 ± 9.71	$2.02 < 3.17 < 4.86$	$6.78 < 7.06 < 7.44$	7.53 ± 0.03
206.....	597.1 ± 19.5	204.1 ± 7.41	21.6 ± 9.20	<1.72	$1.48 < 1.97 < 2.48$	$7.42 < 7.55 < 7.84$	7.75 ± 0.02
208.....	658.0 ± 30.9	249.8 ± 12.3	15.6 ± 8.00	<22.1	$1.16 < 1.56 < 1.93$	$7.67 < 7.85 < 8.22$	7.84 ± 0.03
223.....	242.9 ± 15.3	83.3 ± 7.53	23.7 ± 18.9	...	$1.45 < 4.64 < 19.62$	$6.14 < 6.61 < 7.53$...
252.....	466.8 ± 9.32	157.9 ± 3.57	9.20 ± 4.00	139.0 ± 3.71	$1.16 < 1.45 < 1.72$	$7.68 < 7.87 < 8.14$	7.72 ± 0.01

NOTES.—Only emitters with $>15 \sigma$ H β fluxes are listed. All fluxes are normalized by their $f(\text{H}\beta)$ and multiplied by 100. The 1σ upper limits are listed for [O II] $\lambda 3727$ flux below 3σ and [O III] $\lambda 4363$ below 1σ . The [O III] fluxes are relatively uncertain as discussed in the text. The [O II] $\lambda 3727$ lines of ID 41 and ID 223 are beyond the DEIMOS wavelength coverage.

^a Empirically determined metallicity using R23 based on Yin et al. (2007) shown for comparison. This method generally favors measurements at the upper end of the direct abundance range for galaxies with the lowest abundance determinations. In computing this, we have assumed that the sources lie in the low-metallicity regime.

Given the weakness of the [O III] $\lambda 4363$ lines even in the detected systems and the presence of galaxies without detected [O III] $\lambda 4363$, it is useful to also consider other estimates of the metallicity. For most of the galaxies the line coverage is such that only the R23 indicator of Pagel et al. (1992) is useful. While there has been considerable controversy about the R23 calibration, recent analyses of large samples of local galaxies with well-determined abundances from the direct method have shown a good empirical correlation between R23 and $12 + \log(\text{O/H})$ at low metallicity (Nagao et al. 2006; Yin et al. 2007). Izotov & Thuan (2007) have tested this and found that the Yin et al. (2007) formula

$$12 + \log(\text{O/H}) = 6.486 + 1.401 \log(\text{R23})$$

provided the best match to their sample. We have included the empirically determined abundances from the Yin et al. (2007) formula as the final column in Tables 4 and 5. The uncertainties are computed using the statistical error for the much stronger

[O III] $\lambda 5007$ line and a 10% systematic error for the [O III] $\lambda 4959$ line. The [O II] $\lambda 3727$ line is very weak and the uncertainty in this line has little effect on the errors. We compare the abundances from the two methods in Figure 15. Most of the direct and empirical abundance determinations agree within the 1σ errors, but in general the empirical abundance, as might be expected, favors the upper end of the direct abundance range for the galaxies with the lowest abundance determinations from the direct method. The empirical method places seven galaxies in the XMPG category.

Our discovery rate of XMPGs appears to be significantly higher than those of other surveys. Only 14 new XMPGs have been discovered from the analysis of $\sim 530,000$ galaxy spectra in the SDSS, and they are all located nearby ($z < 0.005$; SDSS DR3, Kniazev et al. 2003; SDSS DR4, Izotov et al. 2006a). At higher redshift, 17 metal-poor [$7.8 < 12 + \log(\text{O/H}) < 8.3$] galaxies with [O III] $\lambda 4363$ detection have been found at $z \sim 0.7$ in the initial phase of the DEEP2 survey of 3900 galaxies and the Team Keck Redshift Survey of 1536 galaxies (Hoyos et al. 2005). But none of these

TABLE 5
LINE FLUXES AND OXYGEN ABUNDANCES FOR NB912-SELECTED USELS

Object	$f([\text{O III}] \lambda 5007)$	$f([\text{O III}] \lambda 4959)$	$f([\text{O III}] \lambda 4363)$	$f([\text{O II}] \lambda 3727)$	$T_e[\text{O III}]$ (10^4 K)	$12 + \log(\text{O/H})$	$12 + \log(\text{O/H})^a$
[O III] Emitters							
3.....	550.9 ± 12.9	187.9 ± 4.91	23.9 ± 7.90	8.6 ± 2.5	$1.74 < 2.20 < 2.71$	$7.26 < 7.43 < 7.65$	7.71 ± 0.02
6.....	588.1 ± 35.1	216.0 ± 14.2	18.4 ± 11.0	52.0 ± 8.6	$1.20 < 1.79 < 2.39$	$7.40 < 7.68 < 8.14$	7.79 ± 0.03
9.....	442.3 ± 15.3	154.7 ± 6.42	<12.3	157.2 ± 6.88	<1.70	>7.70	7.72 ± 0.02
10.....	490.0 ± 11.9	178.7 ± 5.14	13.7 ± 4.40	128.6 ± 5.3	$1.42 < 1.69 < 1.97$	$7.59 < 7.72 < 7.89$	7.74 ± 0.02
17.....	342.5 ± 20.0	129.7 ± 9.29	15.9 ± 9.40	<7.72	$1.41 < 2.26 < 3.28$	$7.03 < 7.22 < 7.70$	7.44 ± 0.03
20.....	418.7 ± 17.4	135.1 ± 6.96	16.8 ± 5.50	24.5 ± 2.45	$1.69 < 2.11 < 2.57$	$7.18 < 7.36 < 7.58$	7.55 ± 0.02
239.....	202.4 ± 10.2	75.6 ± 6.40	<8.20	190.6 ± 10.2	<2.08	>7.34	7.43 ± 0.02
270.....	351.7 ± 15.1	149.7 ± 7.73	12.4 ± 3.40	30.7 ± 2.72	$1.59 < 1.87 < 2.16$	$7.28 < 7.43 < 7.61$	7.50 ± 0.02
H α Emitters							
52.....	589.1 ± 10.0	179.2 ± 3.42	18.3 ± 1.59	<1.56	$1.75 < 1.83 < 1.92$	$7.62 < 7.67 < 7.72$	7.73 ± 0.02
60.....	619.1 ± 33.5	206.7 ± 12.5	10.7 ± 7.77	48.4 ± 8.7	$0.90 < 1.37 < 1.77$	$7.67 < 7.96 < 8.57$	7.81 ± 0.02
266.....	682.8 ± 10.3	217.7 ± 3.57	14.7 ± 2.42	...	$1.40 < 1.52 < 1.63$	<8.3	...

NOTES.—Same as Table 4 but for NB912 emitters. The [O II] $\lambda 3727$ line of ID 266 is beyond the DEIMOS wavelength coverage.

^a Empirically determined metallicity using R23 based on Yin et al. (2007) shown for comparison. This method generally favors measurements at the upper end of the direct abundance range for galaxies with the lowest abundance determinations. In computing this, we have assumed that the sources lie in the low-metallicity regime.

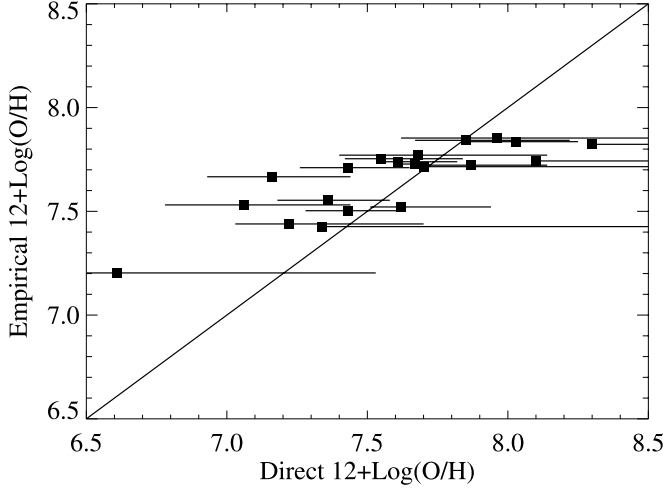


FIG. 15.—Comparison of the direct measurements of $12 + \log(\text{O}/\text{H})$ with those from the empirical method of Yin et al. (2007). Only the much larger error bars for the direct method are shown for clarity. While the abundances derived from the two methods are broadly consistent with the errors, the range of metallicities is smaller when the empirical method is used. This probably reflects the higher accuracy obtained using the strong lines.

galaxies satisfy the condition of XMPGs. Therefore, we conclude that the narrowband method is very powerful for finding not only high-redshift ($z \gg 5$) galaxies but also strong emission line, extremely metal-deficient galaxies at intermediate redshifts ($z < 1$).

Figure 16 shows the electron temperature–sensitive line ratio, $[\text{O III}] \lambda\lambda(4959+5007)/[\text{O III}] \lambda 4363$ versus $[\text{O II}] \lambda 3727/[\text{O III}] \lambda 5007$. If we have an estimate of the metallicity, as in the present case, we can use the $[\text{O II}] \lambda 3727/[\text{O III}] \lambda 5007$ ratio to estimate the ionization parameter q . The ionization parameter q is defined as the number of hydrogen-ionizing photons passing through a unit area per second per unit hydrogen number density (Kewley & Dopita 2002). For the low-metallicity systems with strong $[\text{O III}] \lambda 4363$ lines, we can see from Figure 16 that $[\text{O II}] \lambda 3727$ is very weak compared to $[\text{O III}] \lambda 5007$, with values ranging downward from 0.3. Assuming that the metallicity is less than $0.2 Z_{\odot}$, this would place a lower bound of $q = 10^8 \text{ cm s}^{-1}$ on the ionization parameter based on the Kewley & Dopita (2002) model.

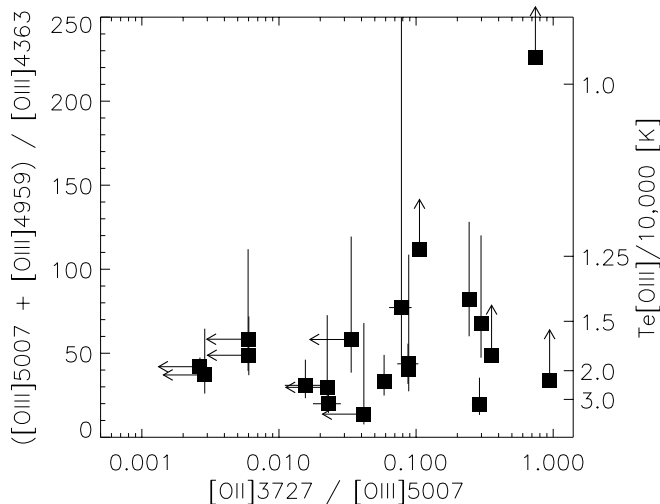


FIG. 16.— $[\text{O III}] \lambda\lambda(4959+5007)/[\text{O III}] \lambda 4363$ vs. $[\text{O II}] \lambda 3727/[\text{O III}] \lambda 5007$ for the $[\text{O III}]$ - and $\text{H}\alpha$ -selected emitters in Tables 4 and 5. The electron temperature of the H II region is also shown.

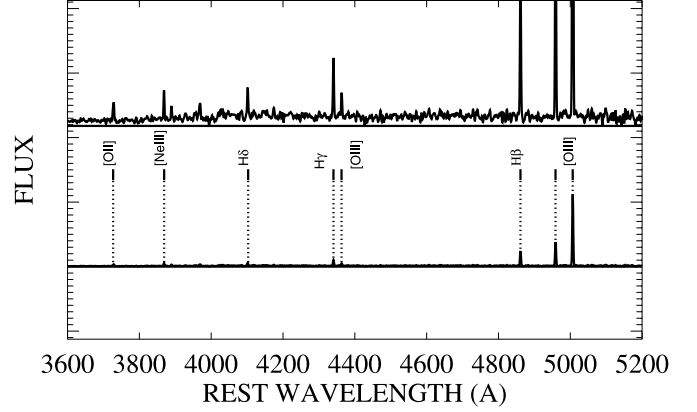


FIG. 17.—Composite spectrum of the eight emitters with $[\text{O II}] \lambda 3727/[\text{O III}] \lambda 5007$ less than 0.1. The eight spectra have simply been summed without weighting. The bottom panel shows the stronger lines, and the top panel shows the continuum and the weaker lines. The stronger emission lines are labeled and marked with the vertical dotted lines.

The higher metallicity objects have stronger $[\text{O II}] \lambda 3727/[\text{O III}] \lambda 5007$, which, while in part due to the metallicity, also requires these objects to have lower ionization parameters, suggesting that we are seeing an evolutionary sequence.

6.2. $\text{H}\alpha$ Emitters

Among 13 $\text{H}\alpha$ emitters in our spectroscopic sample, only three NB912-selected emitters have $\text{H}\beta$ fluxes adequate ($>15 \sigma$) for the purpose of metallicity measurements. Their $T_e[\text{O III}]$ and oxygen abundances were measured using the direct method described above and are shown in Table 5, together with the data for the $[\text{O III}]$ emitters. The $[\text{O II}] \lambda 3727$ line of NB912-selected USEL 266 is outside the Keck DEIMOS wavelength coverage. In order to derive an upper limit on the metallicity, we assumed $[\text{O II}] \lambda 3727/[\text{O III}] \lambda 5007 = 1.0$, which is the maximum value in our sample (see Fig. 16). All our $\text{H}\alpha$ emitters are metal-poor ($Z_{\text{upper}} < 0.45 Z_{\odot}$), but none of them are XMPGs.

6.3. Composite Spectrum

As can be seen in Figure 16, the objects with low $[\text{O II}] \lambda 3727/[\text{O III}] \lambda 5007$ have relatively uniform values of $[\text{O III}] \lambda\lambda(5007+4959)/[\text{O III}] \lambda 4363$ and similar metallicities. Given the relatively low S/N of the individual spectra, it therefore seems of interest to form a composite spectrum. Such a spectrum will have weightings on the lines that depend on the individual ionization parameters and metallicity but will give a rough estimate of the average metallicity and temperature of the sample.

In Figure 17 we show the composite spectrum of the eight objects with $[\text{O II}] \lambda 3727/[\text{O III}] \lambda 5007$ less than 0.1. The $[\text{O III}] \lambda 4363$ line is now strongly detected with a value of 16.7 ± 2.1 , or 8σ . The mean temperature is $19,500 \pm 1500 \text{ K}$, the average abundance is $12 + \log(\text{O}/\text{H}) = 7.5 \pm 0.1$, and the mean rest-frame equivalent width of $\text{H}\beta$ is 57 \AA . The results are similar to the values obtained by averaging the individual analyses of the eight objects.

7. MORPHOLOGIES

The morphology of the USELs may give us a clue to the mechanism of their high star formation activity ($\text{SFR} \sim \text{few } M_{\odot} \text{ yr}^{-1}$) and star formation history; what has triggered the star formation: mergers, gas infall, or galactic winds? High-resolution *Hubble Space Telescope* (HST) Advanced Camera for Surveys (ACS) images are available for the GOODS-North (GOODS-N) region (Giavalisco et al. 2004), which is one of our survey fields. There

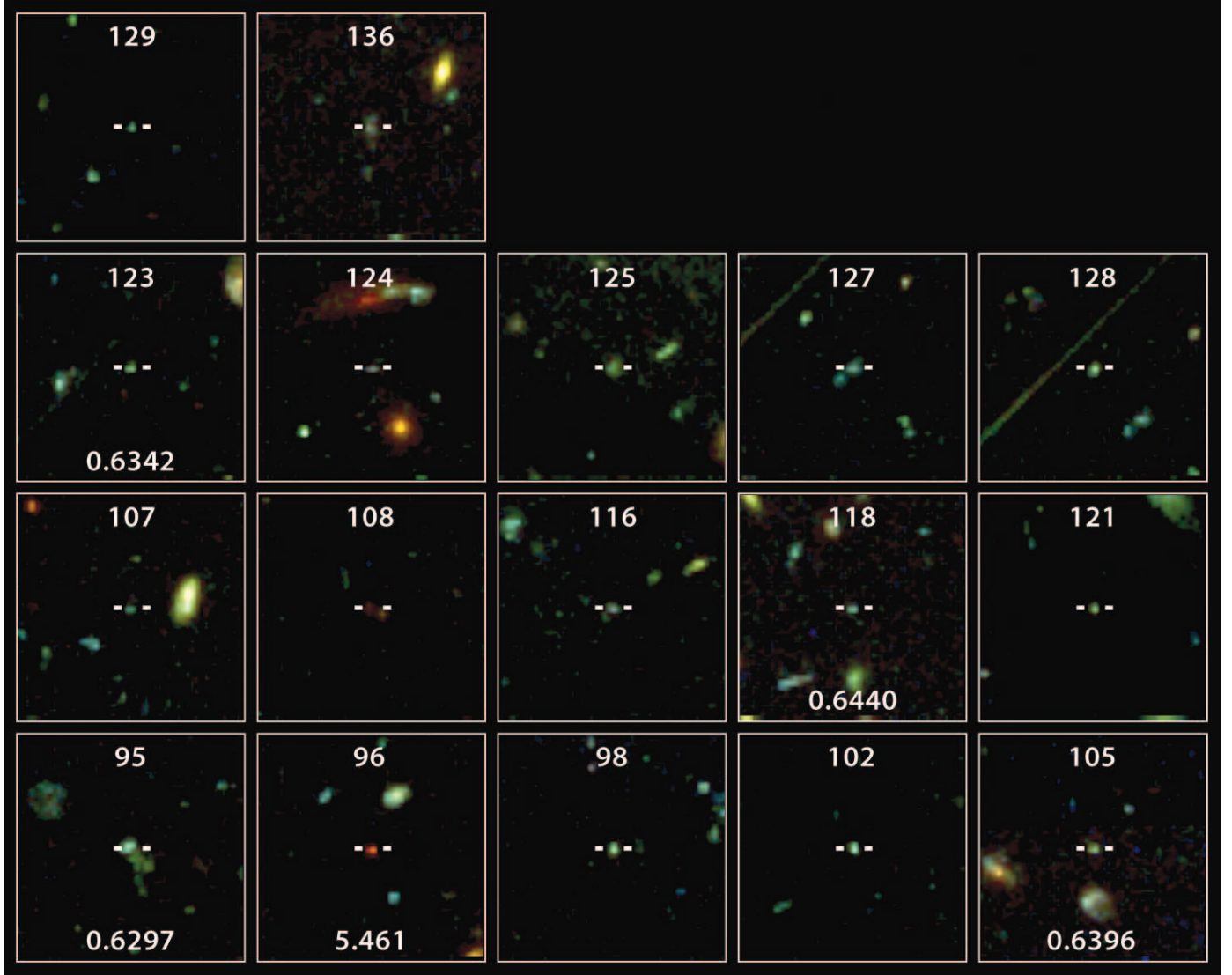


FIG. 18.—*HST* ACS (B , V , z') composite images of NB816 emitters in the GOODS-N field with overlaid object IDs from Table 2 and redshifts, where known. Fields are $12.5''$ on a side.

are 17 NB816-selected USELs in the GOODS-N and 16 in the NB912 sample. Figures 18 and 19 show thumbnails of the NB816- and NB912-selected USELs in the GOODS-N field, respectively, with each thumbnail $12.5''$ on a side. The white dashes point to the galaxy. We used continuum broadband images to show underlying stellar populations: *HST* ACS B -, V -, and z' -band images were used for NB816 emitters, and B -, V -, and I -band images for NB912 emitters. High-redshift $\text{Ly}\alpha$ emitters ($z \gg 5$) are very red because of the continuum absorption below $\text{Ly}\alpha$ emission caused by neutral hydrogen in the intergalactic medium. We do not have spectra for most of the USELs in the GOODS-N field yet, although USEL 118 in the NB816 sample is an XMPG based on both the direct and the empirical methods. However, we can qualitatively argue that the USELs at intermediate redshift ($z < 1$) exhibit widespread morphologies from relatively compact high surface brightness objects to very diffuse low surface brightness ones.

8. DISCUSSION

The present emitters differ from the local dwarf H II galaxies in a large number of ways although they appear much more similar

to the XMPGs found in the SDSS samples. They are much more luminous, have large $[\text{O III}]/[\text{O II}]$ ratios, and are a relatively high fraction (about 10% by number from Fig. 14) of other galaxy populations at these redshifts. Taken together, this suggests that we are seeing much more massive galaxies in the early stages of formation and, since we need these to have relatively long lifetimes in order to understand their frequency, that we are seeing objects undergoing continuous star formation rather than single starbursts. For the case of constant star formation with a standard Salpeter IMF a forming galaxy can have equivalent widths above 30 \AA for 10^9 yr (Leitherer et al. 1999), which would allow us to understand the observed number density of strong emitters relative to the total galaxy population.

In this type of model we would expect the metallicity to grow with time and that higher metallicity galaxies would have higher continuum magnitudes and lower equivalent widths in $\text{H}\beta$. We plot the absolute rest-frame B magnitudes versus the oxygen abundance derived by the direct method in Figure 20. As with the case for the local XMPGs found in the SDSS (*filled circles*; Kniazev et al. 2003; Kewley et al. 2007) and the metal-poor galaxies [$7.8 < 12 + \log (\text{O}/\text{H}) < 8.3$] at $z \sim 1$ (*triangles*; Hoyos

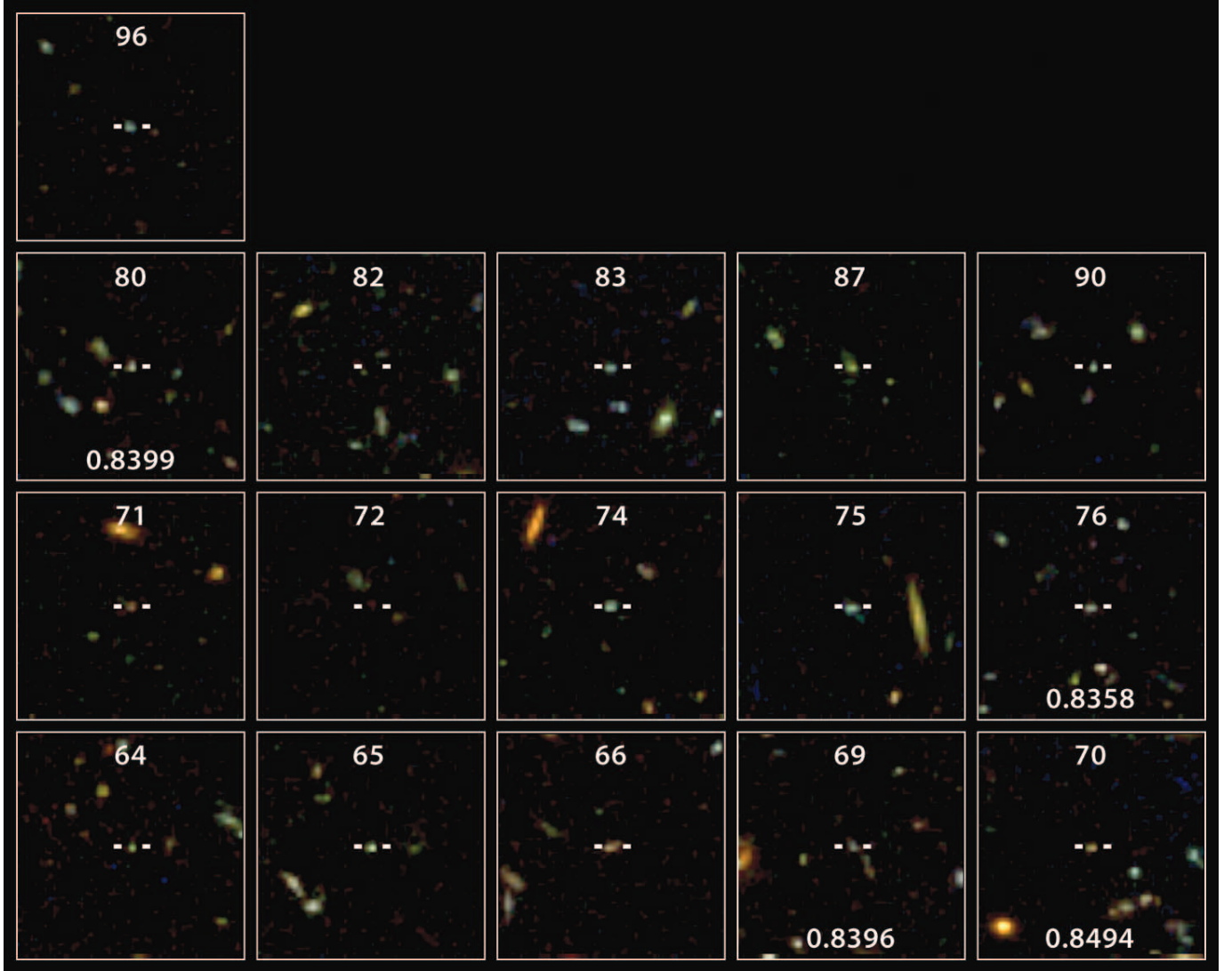


FIG. 19.—*HSTACS* (*B*, *V*, *I*) composite images of NB912 emitters in the GOODS-N field with overlaid object IDs from Table 3 and redshifts, where known. Fields are 12.5'' on a side.

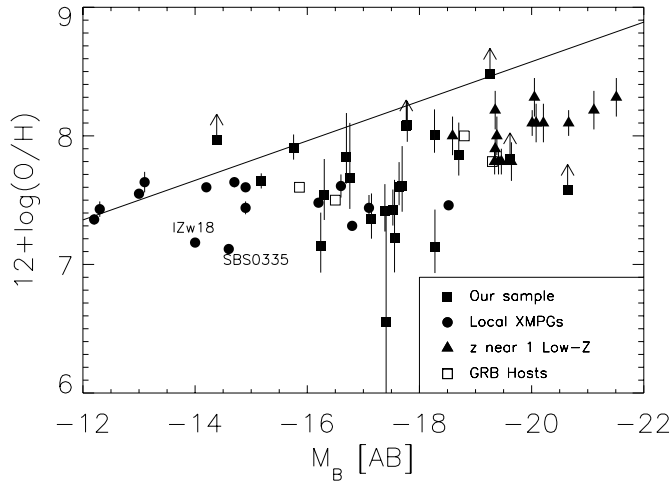


FIG. 20.—Oxygen abundance based on the direct method vs. the absolute rest-frame B magnitude for the $[\text{O III}]$ -selected samples (*filled squares*). The 1σ errors are shown for the oxygen abundances, and 1σ lower limits are shown with upward-pointing arrows. The solid line shows the Skillman et al. (1989) relation for the nearby dwarf irregulars. As with the local XMPGs (*filled circles*; Kniazev et al. 2003; Kewley et al. 2007) and GRB hosts (*open squares*; Stanek et al. 2006; Kewley et al. 2007), the present galaxies are much more luminous at a given metallicity than the local irregulars. Metal-poor luminous galaxies (but not XMPGs) at $z \sim 1$ from Hoyos et al. (2005) are shown as triangles. A few of our emitters may have oxygen abundances comparable to the most metal-deficient galaxies, I Zw 18 [$12 + \log(\text{O}/\text{H}) = 7.17 \pm 0.01$; Thuan & Izotov 2005] and SBS 0335–052W [$12 + \log(\text{O}/\text{H}) = 7.12 \pm 0.03$; Izotov et al. 2005]. [See the electronic edition of the *Journal* for a color version of this figure.]

et al. 2005), the present emitters (*filled squares*) are much more luminous at a given metallicity than is found for the local dIrrs (*solid line*; Skillman et al. 1989). Furthermore, there does indeed seem to be a trend to higher continuum luminosities at higher metallicity consistent with ongoing star formation raising the luminosity. Recently Kewley et al. (2007) reported the similarity between XMPGs and long-duration gamma-ray burst (GRB) hosts; they share similar SFRs and extinction levels, and both lie in a similar region of the luminosity-metallicity diagram. Our sample metal-deficient galaxies, which also lie in the region of GRB hosts, may be additional support of the connection between

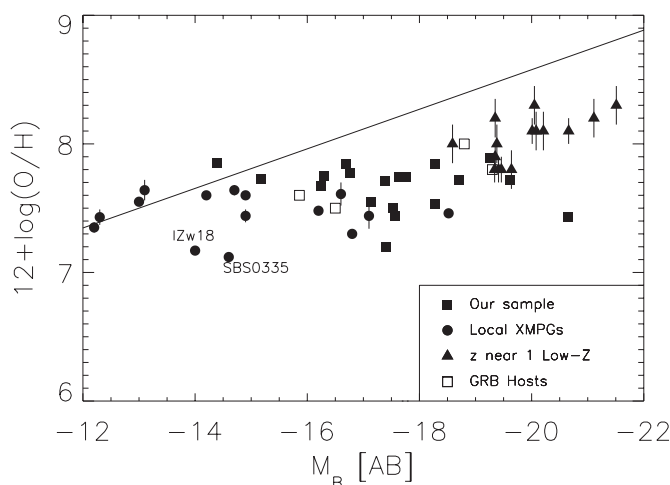


FIG. 21.—Oxygen abundance based on the empirical method vs. the absolute rest-frame B magnitude for the $[\text{O III}]$ -selected samples (*filled squares*). The 1σ errors are shown for the oxygen abundances. The remaining parts of the figure follow Fig. 20. [See the electronic edition of the *Journal* for a color version of this figure.]

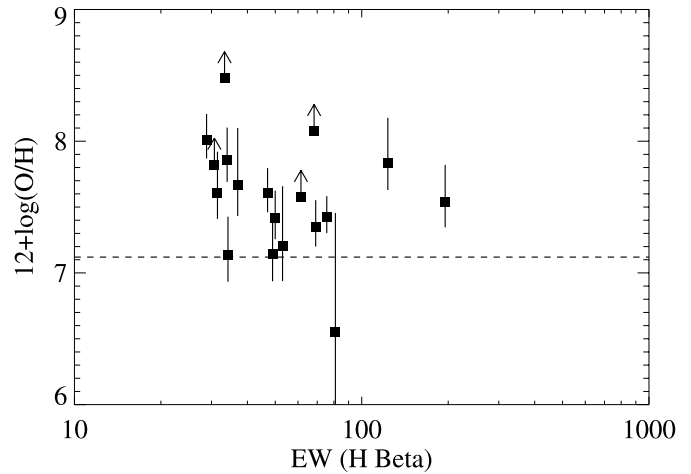


FIG. 22.—Oxygen abundance vs. the rest-frame $\text{H}\beta$ equivalent width for the $[\text{O III}]$ -selected samples. The 1σ errors are shown for the oxygen abundances, and 1σ lower limits are shown with upward-pointing arrows. The dotted line shows the metallicity of I Zw 18.

XMPGs and GRB hosts. Figure 21 shows the same relation, but the oxygen abundance of our sample is based on the Yin et al. (2007) empirical method. Essentially the same trend as Figure 20 can be seen, but now with much smaller error bars in oxygen abundance.

Of the six galaxies with continuum magnitudes brighter than -18 , all but one have metallicities or lower limits that would place them near or above $12 + \log(\text{O}/\text{H}) = 8$, while the lower luminosity galaxies primarily have $12 + \log(\text{O}/\text{H})$ in the range 7.1 – 7.8 . If we assumed that the metallicity were a simple linear function of the age, then the more luminous galaxies would be several times older than the less luminous ones, which is not quite enough to account for the luminosity increase (see, e.g., Leitherer et al. 1999), suggesting that the enrichment process may be more complex. However, the accuracy of our current metallicity measurements may be inadequate for measuring the lowest metallicities in the sample, and we could be underestimating the amount of metallicity evolution.

The relation between the metallicity and the $\text{H}\beta$ equivalent width is shown in Figure 22. There clearly is a large scatter in metallicity at all equivalent widths, suggesting that the star formation may be episodic with periods in which bursts of star formation enhance the $\text{H}\beta$ equivalent widths in objects where previous star formation has raised the metallicity.

With better spectra and more accurate metal estimates we should be able to refine these tests and also determine whether the number density of objects versus metallicity is consistent with that expected in a simple growth model. Perhaps even more importantly, as larger spectroscopic samples are obtained we should be able to determine if there is a floor on the metallicity corresponding to the enrichment in the intergalactic gas. Within the errors we have yet to find an object with lower metallicity than the lowest metallicity local galaxies, but this could easily change as the observations are improved.

9. SUMMARY

We have described the results of spectroscopic observations of a narrowband-selected sample of extreme emission line objects. The results show that such objects are common in the $z = 0$ – 1 redshift interval and produce about 5%–10% of the star formation seen in ultraviolet or emission-line measurements at these

redshifts. A very large fraction of the strong emitters are detected in the [O III] λ 4363 line, and oxygen abundances can be measured using the direct method. The abundances primarily lie in the 12 + log (O/H) range of 7–8 characteristic of XMPGs.

The results suggest that at these redshifts we are seeing early chemical enrichment of start-up galaxies that are forming in relatively chemically pristine regions. As we develop larger samples of these objects and improve the accuracy of their abundance estimates, we should be able to test this model and determine if there is a floor in the metallicity of the galaxies.

We are indebted to the staff of the Subaru and Keck observatories for their excellent assistance with the observations. We particularly thank the Subaru SuprimeCam support astronomer, Hisanori Furusawa, for his help. We would also like to acknowledge invaluable advice on the metallicity measurements from Lisa J. Kewley and Roberto Terlevich and to thank the anonymous referee for an extremely useful report. This material is based on work supported by National Science Foundation grants AST 04-07374 (L. L. C.) and AST 06-87850 (E. M. H.) and by NASA through an award issued by JPL 1289080 (E. M. H.).

REFERENCES

- Ajiki, M., et al. 2003, *AJ*, 126, 2091
 ———. 2006, *PASJ*, 58, 113
 Capak, P., et al. 2004, *AJ*, 127, 180
 Corbin, M. R., Vacca, W. D., Cid Fernandes, R., Hibbard, J. E., Somerville, R. S., & Windhorst, R. A. 2006, *ApJ*, 651, 861
 Cowie, L. L., Songaila, A., Hu, E. M., & Cohen, J. G. 1996, *AJ*, 112, 839
 Faber, S. M., et al. 2003, *Proc. SPIE*, 4841, 1657
 Garnett, D. R. 1992, *AJ*, 103, 1330
 Gialvalisco, M., et al. 2004, *ApJ*, 600, L93
 Hoyos, C., Koo, D. C., Phillips, A. C., Willmer, C. N. A., & Guhathakurta, P. 2005, *ApJ*, 635, L21
 Hu, E. M., Cowie, L. L., Capak, P., Hayashino, T., & Komiyama, Y. 2004, *AJ*, 127, 563
 Hu, E. M., Cowie, L. L., & McMahon, R. G. 1998, *ApJ*, 502, L99
 Izotov, Y. I. 2006, in *ASP Conf. Ser. 353, Stellar Evolution at Low Metallicity: Mass Loss, Explosions, Cosmology*, ed. H. J. G. L. M. Lamers et al. (San Francisco: ASP), 349
 Izotov, Y. I., Papaderos, P., Guseva, N. G., Fricke, K. J., & Thuan, T. X. 2006a, *A&A*, 454, 137
 Izotov, Y. I., Stasińska, G., Meynet, G., Guseva, N. G., & Thuan, T. X. 2006b, *A&A*, 448, 955
 Izotov, Y. I., & Thuan, T. X. 2007, *ApJ*, 665, 1115
 Izotov, Y. I., Thuan, T. X., & Guseva, N. G. 2005, *ApJ*, 632, 210
 Kennicutt, R. C., Jr. 1998, *ARA&A*, 36, 189
 Kewley, L. J., Brown, W. R., Geller, M. J., Kenyon, S. J., & Kurtz, M. J. 2007, *AJ*, 133, 882
 Kewley, L. J., & Dopita, M. A. 2002, *ApJS*, 142, 35
 Kniazev, A. Y., Grebel, E. K., Hao, L., Strauss, M. A., Brinkmann, J., & Fukugita, M. 2003, *ApJ*, 593, L73
 Kobulnicky, H. A., & Kewley, L. J. 2004, *ApJ*, 617, 240
 Kobulnicky, H. A., et al. 2003, *ApJ*, 599, 1006
 Kunth, D., & Östlin, G. 2000, *A&A Rev.*, 10, 1
 Leitherer, C., et al. 1999, *ApJS*, 123, 3
 Lilly, S. J., Carollo, C. M., & Stockton, A. N. 2003, *ApJ*, 597, 730
 Ly, C., et al. 2007, *ApJ*, 657, 738
 Maier, C., Lilly, S. J., Carollo, C. M., Meisenheimer, K., Hippelein, H., & Stockton, A. 2006, *ApJ*, 639, 858
 Melbourne, J., & Salzer, J. J. 2002, *AJ*, 123, 2302
 Miyazaki, S., et al. 2002, *PASJ*, 54, 833
 Nagao, T., Maiolino, R., & Marconi, A. 2006, *A&A*, 459, 85
 Oey, M. S. 2006, in *ASP Conf. Ser. 353, Stellar Evolution at Low Metallicity: Mass Loss, Explosions, Cosmology*, ed. H. J. G. L. M. Lamers et al. (San Francisco: ASP), 253
 Oke, J. B. 1990, *AJ*, 99, 1621
 Osterbrock, D. E. 1989, *Astrophysics of Gaseous Nebulae and Active Galactic Nuclei* (Mill Valley: University Science Books)
 Pagel, B. E. J., Simonson, E. A., Terlevich, R. J., & Edmunds, M. G. 1992, *MNRAS*, 255, 325
 Pilyugin, L. S., & Thuan, T. X. 2005, *ApJ*, 631, 231
 Popescu, C. C., Hopp, U., Hagen, H. J., & Elsaesser, H. 1996, *A&AS*, 116, 43
 Pustilnik, S. A., Engels, D., Kniazev, A. Y., Pramskij, A. G., Ugryumov, A. V., & Hagen, H.-J. 2006, *Astron. Lett.*, 32, 228
 Salzer, J. J., et al. 2000, *AJ*, 120, 80
 Sargent, W. L. W., & Searle, L. 1970, *ApJ*, 162, L155
 Schiminovich, D., et al. 2005, *ApJ*, 619, L47
 Schlegel, D. J., Finkbeiner, D. P., & Davis, M. 1998, *ApJ*, 500, 525
 Seaton, M. J. 1975, *MNRAS*, 170, 475
 Skillman, E. D., Kennicutt, R. C., Jr., & Hodge, P. W. 1989, *ApJ*, 347, 875
 Stanek, K. Z., et al. 2006, *Acta Astron.*, 56, 333
 Stern, D., Bunker, A., Spinrad, H., & Dey, A. 2000, *ApJ*, 537, 73
 Stockton, A., & Ridgway, S. E. 1998, *AJ*, 115, 1340
 Thuan, T. X., & Izotov, Y. I. 2005, *ApJS*, 161, 240
 Tran, K.-V. H., Lilly, S. J., Crampton, D., & Brodwin, M. 2004, *ApJ*, 612, L89
 Ugryumov, A. V., et al. 1999, *A&AS*, 135, 511
 Wilson, G., Cowie, L. L., Barger, A. J., & Burke, D. J. 2002, *AJ*, 124, 1258
 Wyder, T. K., et al. 2005, *ApJ*, 619, L15
 Yin, S. Y., Liang, Y. C., Hammer, F., Brinchmann, J., Zhang, B., Deng, L. C., & Flores, H. 2007, *A&A*, 462, 535